UNIVERSITY OF OKLAHOMA

GRADUATE COLLEGE

FAST SCRAMBLING IN A LONG-RANGE XX/YY/ZZ MEASUREMENT-ONLY QUANTUM CIRCUIT

A THESIS

SUBMITTED TO THE GRADUATE FACULTY

in partial fulfillment of the requirements for the

Degree of

MASTER OF SCIENCE

by HINATA YOKOYAMA

Norman, Oklahoma

2025

FAST SCRAMBLING IN A LONG-RANGE XX/YY/ZZ MEASUREMENT-ONLY QUANTUM CIRCUIT

A THESIS APPROVED FOR THE

HOMER L. DODGE DEPARTMENT OF PHYSICS AND ASTRONOMY

BY THE COMMITTEE CONSISTING OF

Dr. Kieran Mullen, Chair

Dr. Eric R. I. Abraham

Dr. Tomasz Przebinda

ACKNOWLEDGMENTS

I would like to acknowledge my previous advisor, Dr. Bihui Zhu, with whom I had the privilege of conducting my research. She defined the question addressed in the thesis. Her guidance, encouragement, and insightful feedback were instrumental in shaping the direction and depth of this work. I am truly thankful for the opportunity to work under her supervision and to learn from her expertise.

I am also deeply appreciative of Dr. Chenwei Lv, whose code and prior work formed the foundation of much of my computational analysis. His generosity in sharing his resources and his support throughout the project were invaluable.

This research was supported in part by the National Science Foundation grant PHY No. 2317030. I gratefully acknowledge this support.

I would like to thank my committee members, Dr. Kieran Mullen, Dr. Eric R. I. Abraham, and Dr. Tomasz Przebinda, for their time, feedback, and support during the completion of this thesis.

Many thanks also go to my colleagues and friends for their camaraderie, helpful discussions, and encouragement along the way.

Finally, I am forever grateful to my family for their unconditional love and support throughout this journey.

ABSTRACT

This study explores fast scrambling and measurement-induced phase transitions in long-range XX/YY/ZZ measurement-only quantum circuits. Using the stabilizer formalism and Gottesman-Knill theorem, we analyze entanglement growth, quantum information scrambling, and phase transitions in a one-dimensional spin-$\frac{1}{2}$ chain. The results reveal a transition from area-law to volume-law entanglement at a critical probability $P_{YY} = 0.185$ for $\alpha = 2.00$, validated by finite-size scaling analysis. The initial state dependence and the role of long-range measurements are also examined. These findings enhance our understanding of non-equilibrium quantum dynamics and provide insights into their connection with fast scrambling and black hole analogies.

TABLE OF CONTENTS

LIST OF FIGURES

I. INTRODUCTION

There have been extensive attempts to simulate quantum systems through mapping to certain problems of quantum computation. Specifically, the study of non-equilibrium dynamics plays an important role in the realization of quantum computers. Quantum computers are made of qubits and contain interactions between qubits, which may lead to a dynamical phase transition. A phase transition describes a dynamical change in a system after a parameter crosses a critical threshold. This is of great interest because it aids researchers in studying universality classes that categorize system behavior before and after phase transitions (1; 2; 3; 4; 5).

We consider a quantum circuit that consists of only measurements called a Measurement-Only quantum Circuit (MOC). This is in contrast to a circuit which might have a variety of user defined gates that are used to control the time evolution of its components. The dynamics of this circuit have gathered significant attention due to the Entanglement Phase Transitions (EPTs) induced by measurements. The EPTs are characterized by a change in the growth rate of entanglement based on the system size. The system enters the volume-law (area-law) entangled phase where the entanglement growth is linearly dependent(independent) on the increase of the system sizes, crossing a transition point that is responsible for a dynamical change of the system. Furthermore, entanglement grows in different phases as follows:

$$S_A(L) \propto \begin{cases} L & p < p_c, \quad \text{volume law phase,} \\ \log L & p = p_c, \quad \text{critical point,} \\ C & p > p_c, \quad \text{area law phase,} \end{cases}$$

where $S_A(L)$ is bipartite entanglement entropy for subsystem of A with system size of L, which is a measure of quantum correlation between two subregions, and p (p_c) is a measurement rate (critical point). Entanglement grows differently among each phase based on measurement rates ($p < p_c, p = p_c, p > p_c$) in hybrid quantum circuit which consists of random unitary gates and measurements(6).

Interestingly, Jian et al. investigated the critical behaviors of entanglement transition induced by repeated projective measurements in a random quantum circuit (7). In their work, the calculation of the entanglement entropy in such a circuit is mapped onto a two-dimensional mechanics problems which is solvable by Conformal Field Theory (CFT)(8). The conformal transformation is a coordinate transformation that is a local rescaling of the metric (9). This transition point can be mapped to a percolation critical point in the replica and semi-classical limits in which percolation refers to a classical probability problem of understanding how random occupation of sites or bonds in a lattice leads to the formation of connected clusters (10) (1). The dynamics of the measurement induced phase transition is also described by statistical models.

Furthermore, EPTs are well studied within random tensor networks in which tensors represent connections of particles in a system(2; 7). This method is often used to investigate properties of many-body physics and statistical mechanics(11). For example, EPT is utilized to determine the properties of quantum many-body systems built by holographic tensor networks(2). Such systems transition from the many-body localization (MBL) phase to Eigenstate Thermalization Hypothesis (ETH) phase(12; 13). MBL is a quantum phenomenon in which a single particle is unable to move on a lattice with random on-site energy, and it fails to reach thermal equilibrium even after a long time of system evolution. The information of initial conditions is preserved (14; 15). The MBL phase satisfies an area-law scaling. On the other hand, ETH states that the reduced density matrices of small subsystems are thermal. This implies that the ETH phase satisfies a volume-law scaling.

In addition, scrambling, the spreading of quantum information across an entire system, is investigated in this work. When a system is scrambled, its quantum information is not accessible to local measurements because it is distributed throughout the system(6). The dynamics of strongly interacting systems lead to the fast loss of initial conditions, similar to classical chaotic behaviors(16). This scrambling process is highly correlated with thermalization and chaos in quantum systems(17) and shows volume-law entanglement behaviors associated with unitary black holes(4). The tensor network geometric structure of volume-law entanglement is called 'black hole'(2). The scrambling is experimentally observed in Landsman's group(18). They used Out-of-Time-Ordered correlation function (OTOC) to characterize quantum information scrambling in a quantum circuit. As scrambling proceeds, the OTOC decays(19).

Moreover, the existence of a maximum speed of scrambling called "fast scrambling" can be seen in the propagation of quantum information. This concept was introduced by Lieb and Robinson in 1972(20). They proposed that there is a finite velocity of quantum information spreading. Analogous to Einstein's relativity(21), this phenomenon can be described as a "light cone" for information spreading. For power-law interactions a typical form for non-relativistic long-range interactions such as the Coulomb interaction and the dipole-dipole interaction, $\propto \frac{1}{r^{\alpha}}$, the Lieb Robinson bound depends on dimension of the system and the exponent of α(22). The long-range unitary interaction induces scrambling effects(23). The strong long-range property of two-body measurements dramatically changes the linear-light-cone propagation of entanglement entropy while the short-range suppresses the behavior(3).

This paper summarizes the progress of the fast scrambling in a long-range $XX/YY/ZZ$ MOC and examines the properties of measurement-only dynamics. In the following sections, we describe the methodology, including Gottesman-Knill theorem and stabilizer formalism, and the model of the measurement-only dynamics including the diagram in II. Methodology and III. Model. The results of the MOC are discussed in IV. Results and V. Discussion. The measurement-induced EPT is confirmed around the transition, and we identify the crossing points of the Tripartite Mutual Information across different system sizes using finite-size scaling analysis. The growth of entanglement entropy is fitted using numerical techniques, which follows the scaling above. In addition, the initial state dependence and propagation of scrambling are studied. We find that the quantum information spreads over the entire system once the system is in the volume-law regime and the sign of the Tripartite Mutual Information is negative. This feature is observed as a step function like behavior. We also see "light cone" of propagation of the quantum information. Finally, we summarize the results and relate them to any future work in VI. Summary. Supplementary information is available in Appendix.

II. METHODOLOGY

2.1 Gottesman-Knill theorem

First, we introduce the Pauli group, consisting of 16 matrix elements, including the identity matrix and all Pauli matrices. Pauli matrices are a set of 2×2 and complex Hermitian and unitary matrices:

$$X = \begin{pmatrix} 0 & 1 \\ 1 & 0 \end{pmatrix}, \quad Y = \begin{pmatrix} 0 & -i \\ i & 0 \end{pmatrix}, \quad Z = \begin{pmatrix} 1 & 0 \\ 0 & -1 \end{pmatrix}.$$

The Pauli group is defined as :

$$\mathscr{P} \in (\pm I, \pm iI, \pm X, \pm iX, \pm Y, \pm iY, \pm Z, \pm iZ) \tag{1}$$

where I is an identity operator. An n-element Pauli operator is referred to as a “Pauli string.”

$$\mathscr{P}_n = \{P_1 \otimes, \ldots \otimes P_n | P_1 \ldots P_n \in \mathscr{P}\}. \tag{2}$$

The Gottesman-Knill theorem suggests that a quantum circuit consisting solely of $CNOT$, Hadamard, and phase gates can be simulated efficiently on a classical computer(24). These gates are defined as:

1. Hadamard Gate:

$$H = \frac{1}{\sqrt{2}} \begin{pmatrix} 1 & 1 \\ 1 & -1 \end{pmatrix},$$

2. Phase Gate:

$$S = \begin{pmatrix} 1 & 0 \\ 0 & i \end{pmatrix},$$

3. Controlled-NOT (*CNOT*) Gate:

$$\text{CNOT} = \begin{pmatrix} 1 & 0 & 0 & 0 \\ 0 & 1 & 0 & 0 \\ 0 & 0 & 0 & 1 \\ 0 & 0 & 1 & 0 \end{pmatrix},$$

These gates are called Clifford gates, which transform a Pauli string into another Pauli string. In other words, Clifford gates are elements of the Clifford group that satisfies $C_n = \{T \in U_{2^n} | T\mathscr{P}T^{\dagger} = \mathscr{P}\}$ where C_n is n-qubit Clifford group. Note we call a circuit unitary if it does not contain measurement gates(24).

2.2 Stabilizer formalism

One class that is introduced to analyze quantum error-correcting codes is called stabilizer circuits(25). A stabilizer circuit is a quantum circuit which implemented by *CNOT*, Hadamard, phase gates, and a single-qubit measurement gate. We call the stabilizer circuit unitary if it does not contain measurement gates. Unitary stabilizer circuits are also known as Clifford group circuits. A quantum state of a stabilizer satisfies

$$S|\psi\rangle = (+1)|\psi\rangle, \tag{3}$$

where $|\psi\rangle$ is a stabilizer state. We say that S stabilizes the subspace of V if S stabilizes every state in V. The largest subspace of a set of stabilizers is called the stabilizer subspace. In other words, an operator of S stabilizes a quantum state if $|\psi\rangle$ is an eigenstate of S with its eigenvalue of +1. It is important to note that we need to take care of global phase factors. If $S|\psi\rangle = -|\psi\rangle$, we do not say that the operator stabilizes the state(26). This means that $|\psi\rangle = 0$.

Stabilizer groups are a subgroup of P_n and abelian and do not contain $-I$. An element which belongs to stabilizer groups is called a Pauli stabilizer. Since all Pauli strings square to the identity and pairs of Pauli strings either commute or anti-commute, this implies that Pauli strings must commute in order to stabilize the state. In this paper, we apply the measurement algorithm in Ref (27).

1. Identify $M \in S$ in the stabilizer generators satisfying $\{M,A\} = 0$ (where $[M,A] \neq 0$) where A is a measured Pauli string.

2. For each N, where N runs over the other generators of S:

   - Leave N alone if $[N,A] = 0$,
   - Replace N with MN if $\{N,A\} = 0$ (by calling the row sum operation),

   such that all stabilizer generators now commute with A except for M.

3. Replace M by $+A$ or $-A$ in the stabilizer generator.

where $[N,A] = NA - AN$ and ($\{M,A\} = MA + AM$) denotes the (anti) commutator.

2.3 Density matrix

Given an operator S that stabilizes a quantum state of $|\psi\rangle$, then,

$$\frac{1+S}{2}|\psi\rangle = |\psi\rangle, \frac{1-S}{2}|\psi\rangle = 0. \tag{4}$$

If S is a Pauli string, $S^2 = 1$ which makes $\frac{(1+S)}{2}$ a projection operator. The pure state density matrix that is stabilized by an operator of S is defined as (28)

$$|\psi\rangle\langle\psi| = \prod_{k=1}^{L} \frac{I+g_k}{2} = \frac{1}{2^L}\sum_{g\in S} g, \tag{5}$$

where $g_{k=1,\ldots L}$ is a set of stabilizer generators of S and L is the number of qubits. It is clear that the density matrix is the product of the projection operator from the stabilizer generator.

The stabilizer formalism also allows one to calculate they dynamics of a mixed density matrix. The mixed state density matrix is represented as product of projection operators (28):

$$\rho = \frac{1}{2^{N-K}} \prod_{k=1}^{K} \frac{1+g_k}{2}.$$

where K is the number of stabilizer generators.

Those calculations need the multiplication of $2^L \times 2^L$ matrices, which is impractical for large L. The more efficient calculation is discussed in the following section.

2.4 Stabilizer tableau and its multiplication

To implement a stabilizer algorithm, it is convenient to introduce an $L \times (2L+1)$ binary matrix, or a stabilizer tableau. Each row represents an independent generator of a stabilizer group, while $2L$ column represents a Pauli matrix encoded by binary codes, and one column shows the overall sign of the stabilizer generators (± 1.) The binary code for an identity matrix and each Pauli matrix is as follows: $00, 01, 10, 11$ for I, Z, X, and Y, respectively. Therefore, we can define a Pauli string of length L as

$$S = i^{r_0 + x_1 z_1 + \ldots + x_L z_L} X_1^{x_1} Z_1^{z_1} \otimes \ldots \otimes X_L^{x_L} Z_L^{z_L}, \tag{6}$$

where $x_i z_i = 0,1$ and $r_0 = 0,2$ ($r_0 \neq 1,3$ according to Hermiticity). Note that we can express every Pauli matrix by multiplication of X and Z. For example, $X_i^1 Z_i^1 = -iY_i$ and for a trivial case, $X_i^0 Z_i^0 = I_i$. By using these conventions, we can uniquely assign a Pauli string in the form of 2L+1 binary row matrix such as $(r, x_1 z_1, x_2 z_2, \ldots, x_L z_L)^T$. Note that we can ignore the phase term of i^r without affecting any results from stabilizer algorithm since all the quantities that we measure in this work depend on the number of linearly independent stabilizer generators as explained in the following subsection.

Since stabilizers must commute, there are many degrees of freedom in choosing a set of stabilizer generators. However, each stabilizer generator must be linearly independent.

By multiplying one stabilizer generator with another, the linearly independence and the associated stabilizer groups are unaffected. Due to this property, we are free to perform a row summation operation. The rule of row summation operation is described below.

The update rules for x_{cj} and z_{cj} are given by:

$$x_{cj} = x_{aj} \oplus x_{bj}, \tag{7}$$

$$z_{cj} = z_{aj} \oplus z_{bj}. \tag{8}$$

The sign change of the Pauli string needs to be accounted for by:

$$r_c = r_a \oplus r_b \oplus \frac{1}{2} \sum_{j=1}^{L} g(x_{aj}, z_{aj}, x_{bj}, z_{bj}) \mod 4, \tag{9}$$

where the function $g(x_1, z_1, x_2, z_2)$ takes care of the i signs in the multiplication table of Pauli matrices. Explicitly, we have:

$$g(x_1, z_1, x_2, z_2) = \begin{cases} 0 & \text{if } x_1 = 0, z_1 = 0, \\ z_2(2x_2 - 1) & \text{if } x_1 = 1, z_1 = 0, \\ x_2(1 - 2z_2) & \text{if } x_1 = 0, z_1 = 1, \\ z_2 - x_2 & \text{if } x_1 = 1, z_1 = 1, \end{cases}$$

(24).

2.5 Row-Reduced Echelon Form (RREF)

Clifford unitary dynamics can be implemented as column operation of a stabilizer tableau known as Clifford normal form (CNF form). We can also apply the measurement of observables discussed in the previous section . One example of a two-qubit system with stabilizer generators XZ and $-YY$ is written as

$$\left[\begin{array}{cccc:c} 1 & 0 & 0 & 1 & 0 \\ 1 & 1 & 1 & 1 & 1 \end{array}\right].$$

The dashed line distinguishes Pauli operators and sign of a stabilizer generator. The first row can be interpreted as $XZ-$ since 10 corresponds to X, 01 corresponds to Y, and the last digit to the right of the dashed line is 0 which represents $-$. Similarly, we can read the second row as $YY-$ from the left to the right. Again, we emphasize that we ignore the sign (phase term) of each stabilizer generator for numerical calculation without affecting any numerical results.

After we put stabilizer generators into a tableau, we can change it to a normal form known as a Row-Reduced Echelon Form (RREF) and compute its rank. The RREF is obtained through row operations, which do not change stabilizer groups. The algorithm is elaborated below(28).

First, we need to define the active region, which is a rectangular region with the upper-left corner labeled by row K_U, column N_L. Initially, $K_U = 1$, $N_L = 1$. Using row permutation, we sort the rows to make the first column in the active region have "1" before "0". Then, we take into account four cases:

1. There are no "1"s in column N_L.

   (i) Increase N_L by 1.

2. There is only one kind of Pauli operators, which should appear in row K_U.

   (i) Multiply row K_U with all other rows in the active region that have the same Pauli matrices in column N_L.

   (ii) Increase K_U and N_L by 1.

3. There are two kinds of Pauli operators. The first should appear at row K_U. Label the row where the second kind first appears as $K_U + k$.

(i) Multiply row K_U and K_U + k with all other rows in the active region that have the same Pauli matrices in column N_L.

(ii) Sort the rows in the active region again.

(iii) Increase K_U by 2 and N_L by 1.

4. There are three different kinds of Pauli operators. The first kind should appear at K_U. Label the row where the second kind first appears as $K_U + k$. Label the row where the third kind first appears as $K_U + k_1 + k_2$.

(i) Multiply row K_U, $K_U + k_1$, and $K_U + k_2$ with all other rows in the active region that have the same Pauli matrices in column N_L.

(ii) Sort the rows in the active region again.

(iii) Multiply row K_U and $K_U + 1$ with $K_U + 2$.

(iv) Increase K_U by 2 and N_L by 1.

Practically, we use row operations to eliminate Pauli matrices in each column from the left top of the corner of the tableau and minimize the number of Pauli matrices. Afterward, we end up with all identities (zeros) in the left lower triangular region (RREF).

2.6 Entanglement entropy

Entanglement entropy is a measure of the degrees of quantum entanglement between two subsystems. The bipartite Von Neumann entanglement entropy is defined as

$$\mathscr{S}(\rho_A) = -Tr(\rho_A log_2(\rho_A)), \tag{10}$$

where A is the subsystem and its complement part is $\bar{A}$. The reduced density matrix of A is expressed in terms of the total density matrix $\rho_A = Tr_{\bar{A}}(\rho_{A\bar{A}})$. When the system is in a pure state, $\rho_{A\bar{A}} = |\psi\rangle\langle\psi|_{A\bar{A}}$, the bipartite entanglement entropy becomes the same for the subsystems of A and $\bar{A}$, $\mathscr{S}_A(\rho_A) = \mathscr{S}_{\bar{A}}(\rho_{\bar{A}})$.

Using a stabilizer algorithm, the formula for computing bipartite entanglement entropy is modified. In the stabilizer formalism, the entanglement entropy is directly related to the number of linearly independent stabilizer generators if we truncate the stabilizer generators to the subsystem(29). Let us define $K_{\bar{A}}$ as the number of linearly independent stabilizers restricted to the subsystem $\bar{A}$. $K-K_{\bar{A}}$ is the minimal number of stabilizer generators that only have support within A. This set of stabilizer generators generates the reduced density matrix of ρ_A. The entanglement entropy can be calculated as follows:

$$S_A = |A| - (K - K_{\bar{A}}) = (L-K) + (K_{\bar{A}} + |\bar{A}|), \tag{11}$$

wher $|A|$ is the number of particles in a subsystem of A. By putting the column order of a stabilizer tableau as $\bar{A}, A$, we can read the number of linearly independent stabilizer generators from the RREF. When we have $K = L$, Eq.11 becomes changed for a pure state

$$S_A = K_{\bar{A}} - |A| = K_{\bar{A}} - |\bar{A}| = S_{\bar{A}}. \tag{12}$$

2.7 Multipartite entanglement entropy

In the case of more than two subsystems, we consider multipartite entanglement entropy. We introduce mutual information (MI), which describes mutual dependence of entanglement between subsystems of A and B

$$MI(A,B) = S_A + S_B - S_{AB} = -K + (K_{\bar{A}} + K_{\bar{B}} + K_{\overline{AB}}), \tag{13}$$

where S_{AB} is entanglement entropy of the subsystem consisting of A and B. Note the entire system is equally divided into four regions, A, B, C, and D, for this work where $|A| = |B| = |C| = |D| = \frac{L}{4}$. Due to the subadditivity of entanglement entropy, Eq.13 ≥ 0.

Moreover, we take into account multipartite entanglement entropy for three subsystems of A, B, and C called tripartite mutual information (TMI)

$$
\begin{aligned}
TMI &= S_A + S_B + S_C - S_{AB} - S_{BC} - S_{CA} + S_{ABC} \\
&= -K + (K_{\overline{ABC}} + K_{\bar{A}} + K_{\bar{B}} + K_{\bar{C}} - K_{\overline{AB}} - K_{\overline{BC}} - K_{\overline{CA}}),
\end{aligned} \tag{14}
$$

where S_{BC} and S_{CA} are entanglement entropy of subsystems of B and C and C and A, respectively. This quantity is used to describe quantum information scrambling which was originally proposed as a way to reconcile the impossibility of retrieving information with the fact that quantum information is not destroyed (4). The negative TMI serves as an indicator of a strongly interacting system, and the system with negative TMI is called a monogamy in connection with black hole entanglement(30; 3). These quantities such as the entanglement entropy, MI, and TMI, are investigated to explore the features of the measurement-only circuit.

III. MODEL

We consider a quantum circuit that consists of only measurements of a one-dimensional chain of spin 1/2 particles with length L called a Measurement-Only quantum circuit (MOC) in Fig. 1. In this work, we utilized projective measurements for the site of $i-$th and $j-$th qubits under open boundary conditions; $M_{i,j} = X_i X_j, Y_i Y_j$, and $Z_i Z_j$ where X_i,Y_i, and Z_i are Pauli matrices for the $i-$th and $j-$th sites. Each measurement is conducted by probabilities as follows

$$P_{X_iX_j} = \frac{p_{xx}}{\mathcal{N}|i-j|^{\alpha}}, P_{Y_iY_j} = \frac{p_{yy}}{\mathcal{N}|i-j|^{\alpha}}, P_{Z_iZ_j} = \frac{p_{zz}}{\mathcal{N}|i-j|^{\alpha}}, \tag{15}$$

where $p_{xx}, p_{yy}, p_{zz} \in [0,1]$ are the relative probabilities taking measurements of XX, YY, and ZZ, respectively, and α is a parameter for the range of measurements (Here, we define $\alpha \leq 2$ as long-range measurement and $\alpha > 2$ short-range measurement). In this paper, the probability of taking XX and ZZ is the same: $p_{XX} = p_{ZZ}, p_{YY} = 1-(p_{XX}+p_{ZZ}) = 1-2p_{XX}$ such that $P_{XX}+P_{YY}+P_{ZZ} = 1$. A normalization constant of $\mathcal{N}$ is introduced such that one measurement is taken for each step. For each time step, the types of measurements are chosen randomly and the outcomes of the observables are averaged over a sufficient number of them. We measure entanglement entropy, MI, and TMI to explore the properties of the MOC in terms of phase transition, initial state dependence, and scrambling. Those results are in the following chapter.

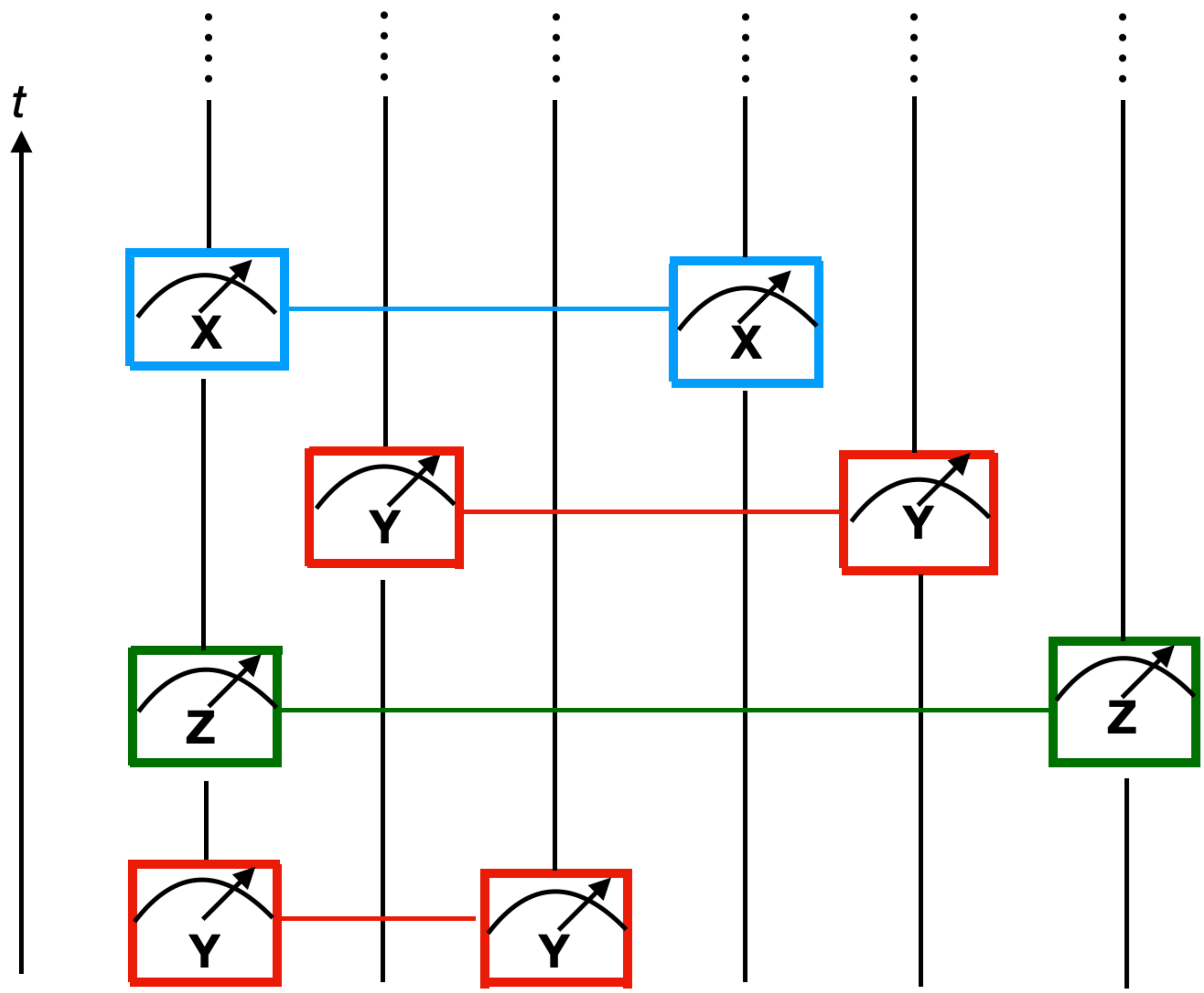

Figure 1: The long-range $XX/YY/ZZ$ measurement-only quantum circuits. For each time step, one of the measurements are randomly chosen at fixed rate. The probability distribution is determined by changing the relative probabilities of p_{xx}, p_{yy}, p_{zz}.

IV. RESULTS

4.1 Phase transitions

In Fig. 2a and Fig. 2b, we plotted the measured saturated value of TMI evolved from the Greenberger-Horne-Zeilinger (GHZ) state with different probabilities P_{YY}. The general form of an n-qubit GHZ state is:

$$|\mathrm{GHZ}\rangle = \frac{1}{\sqrt{2}}\left(|0\rangle^{\otimes n} + |1\rangle^{\otimes n}\right).$$

where $|0\rangle$ and $|1\rangle$ are the eigenstates of Z measurement. The GHZ states are entangled states and their stabilizers are pairwise Z-stabilizers:

$$Z_1Z_2, Z_2Z_3, \ldots, Z_{n-1}Z_n,$$

where Z_i represents the Pauli-Z operator acting on the ith qubit, and the global X-stabilizer:

$$X_1X_2\cdots X_n,$$

where X_i represents the Pauli-X operator acting on the ith qubit. As α decreases, the qubit pairs separated at a certain distance are more likely to be chosen and contribute to the TMI values. In addition, the minimum values of TMI in Fig.2 are located at the same probability of each measurement such as $P_{XX} = P_{YY} = P_{ZZ} = \frac{1}{3}$. This means that the final state is clusters of X, Y, and Z of stabilizer states and their sizes are almost equal. Fig.3a shows the linear dependence of TMI on the system sizes with the same probabilities of each measurement. The value of TMI increases when α decreases. In this sense, the curve of TMI gets deeper in the plot as α decreases in the long-range measurements and the system displays strong interaction. The half chain entanglement entropy (HCEE) with the same probability of each measurement is in Appendix A.2 Half Chain Entanglement Entropy. Fig. 3b shows the density plot of TMI with respect to P_{YY} and α with $L = 384$ at $t = 40L$. The results are averaged over 3000 outcomes, and the TMI becomes negative as P_{YY} gets close to $\frac{1}{3}$ and α decreases. The strong negative region indicates that the system is in the volume-law while the "zero-region" implies that the system is in the area-law.

More importantly, the transition point of TMI is seen from the positive and the negative regions in Fig.4b with P_{YY} between 0.1 and 0.2. We take a closer look at the TMI with more finite values of P_{YY} to find the location of the transition point in Fig. 4a. These curves intersect at $P_{YY} = 0.185$, and the TMI with the larger system has more negative TMI values after the transition point. Moreover, finite-size scaling analysis, which assumes a power-law behavior about a critical transition value for P_{YY} and optimizes an initial set of scaling parameters that enforce a data collapse of the different data sets (31), is conducted with $P_{YY} = 0.185$ in Fig. 4b. The scaling ansatz is defined as :

$$TMI(P_{YY}, L) \approx F[(P_{YY} - P_{YYc})L^{\frac{1}{\nu}}]. \tag{16}$$

where P_{YYc} is a critical point responsible for the phase transition and can be used to estimate the value of the critical exponent of ν. The data collapses indicating a universal transition when the correct ν is chosen for P_{YYc}(32). For $P_{YY} = 0.185$ and $\alpha = 2.0$ the corresponding value of ν is 1.1 (Fig. 4b); more details can be found in A.3 Finite-size scaling analysis. We confirm that there is a transition at $P_{YY} = 0.185$ as the data collapses in Fig.4b.

Let us explore what happens around the transition point. Fig.5a shows HCEE with the probabilities $P_{YYc} \pm 0.1$ to observe the EPTs. We fit the curve to the data points. For $P_{YY} = 0.185$ before the transition point (blue curve), an area-law entanglement can be seen, indicating that entanglement entropy in the system is not dependent on the system size. At the critical point(orange curve), the entanglement grows logarithmically. After the transition point with $P_{YY} = 0.285$ (green curve), we can see the entanglement volume-law in which entanglement entropy grows linearly over the system size. Combining the results from Fig.3b, we observe that after the transition point, the TMI becomes negative, indicating that the system transitions to a volume-law phase characterized by strong interactions between its qubits. The EPT with respect to TMI is depicted in Fig.5b. If a system is in area-law phase(volume-law phase), TMI is positive (negative).The arrow represents an increase of measurement rate of p.

4.2 Initial state dependence

We also investigate the initial state dependence of the MOC. In Fig. 6, we plotted the dynamics of TMI with different initial states: the GHZ,$|GHZ\rangle$ (dashed lines) and the product states (solid lines). Since the GHZ are entangled, the TMI starts with 1 while the product of stabilizer states starts with 0. As time goes on, the gap of the TMI vanishes in Fig.6a because the measurements of each gate are chosen almost equally ($P_{XX} = P_{ZZ} = 0.35, P_{YY} = 0.3$). Due to this probability distribution, the initial states change quickly and the TMI value is saturated after $t = 20L$. Therefore, the TMI of the GHZ of Z states does not differ from the product of X/Y/Z stabilizer states.

However, the TMI gap still exists after the simulation is expanded to $t = 40L$ in Fig.6b ($P_{XX} = P_{ZZ} = 0.15, P_{YY} = 0.7$). This occurs because the measurement of the Y operator is more likely to happen than other measurements and does not change the initial state, which does not contribute to the TMI. We believe that the solid line will meet the dashed line when we consider an exponentially long time to run the MOC because of the low probabilities of other projective measurements. Evidently, Fig. 7 shows that the gap of TMI vanishes after a long time of measurements. This means that the gap remaining among the states is temporary and not permanent.

There is a peak at the early time with the dashed line. This occurs because of the high probability of the measurement of the Y operator, which contributes to the sudden peak of the TMI. The magnitude of the peak varies depending on the strength of α. If α is decreased, the magnitude of the peak increases.

4.3 Scrambling

We measured the time evolution of MI between the isolated qubit and the entire system with $L = 256$ in Fig. 9. First, we choose an isolated qubit from the system that is entangled with the qubits located at the center of the one-dimensional lattice we call the 0-th qubit, and run the MOC without measuring the isolated qubit in Fig. 8. All qubits except for the 0-th spin are prepared to be the Y initial stabilizer states and the $0-$th spin and the isolated spin are an EPR pair, $|00\rangle + |11\rangle$. We label each qubit from the 0th qubit. For example, we start counting the qubits to the right of the 0th qubit as n=1,2,3,...L/2 and the qubits to the left of the 0th qubits as $n = -1, -2, -3, ..., -L/2$. MI is calculated as follows:

$$MI(R, [-n, +n]; t) = S_R(t) + S_{[-n,+n]}(t) - S_{R\cup[-n,+n]}(t), \tag{17}$$

where n is the number of sites ($-127 \leq n \leq 127$) at $L = 256$, $[-n, +n]$ is a region of qubits from $-n$ to $+n$, and R is a reference qubit. Note that in this setting, MI is maximized when $t = 0$.

In Fig.9, we observed the propagation of the quantum information with different α and P_{YY}. We can see the thick blue regions in which the MI is almost 0 from the 0-th qubit to ± 60th qubit sites. The hidden MI is revealed in the existence of an outer layer of thick blue regions in Fig. 9a, b, and e. The propagation of quantum information is indicated by the slope starting from the 0-th qubit. Due to the shape of the "light cone", Fig.9e has slower propagation of the quantum information than Fig.9a and Fig.9b. As α increases, the shape of the "light cone" becomes sharper in the long-range measurements (Appendix A.5 Supplemental data for scrambling) On the other hand, it is difficult to determine propagation of the quantum information in 9 c,d, and f. This occurs because we can see scrambling effects in the volume-law region(3), and the area-law phase has the disordered system where the system does not show strong correlation. The shapes of 'light cone' in long and short range measurements are shown in A.5 Supplemental data for scrambling as well as their speeds.

Additionally, we measured the saturated value of MI between the isolated qubit and the entire system for each site at $t = 20L$ in Fig.10. Each color line shows the MI for the different system sizes from $L = 64$ to $L = 512$. We can see a step function in Fig. 10 a,b, and e. The MI is zero until half the size of the system ($n = \pm 0.25$); afterward, the system rapidly emits the quantum information when the system is considered more than half the size of the system. This behavior is seen as a step function in Fig. 10 a,b, and e. We believe this is a sign that the system is scrambled since the quantum information spreads over the entire region, and such a system shows the volume-law entanglement. Furthermore, the sign of TMI becomes negative after the phase transition occurs in Fig. 5b. This means that the negative sign of TMI is also an indicator of scrambling. We can also notice that the strength of the scrambling differs by the depth of the step function. In other words, the strength of the scrambling is $b \geq a \geq e$. In contrast, we do not see scrambling in Fig.10 c,d, and f. Those shapes do not resemble a step function because they are in the area-law phase.

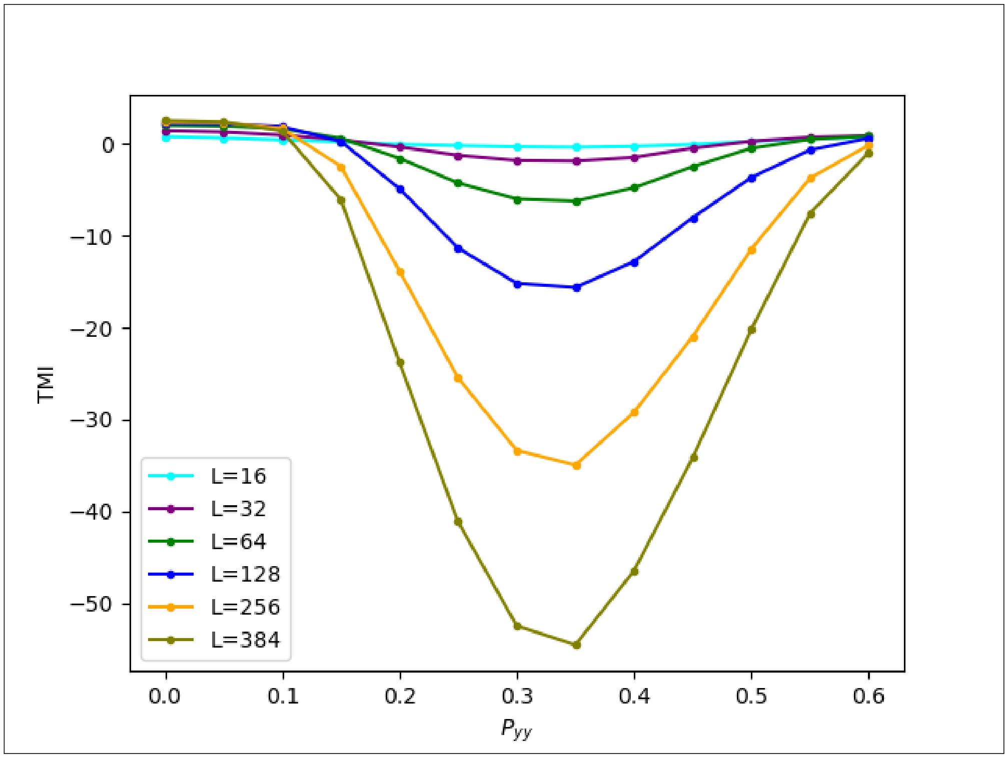

(a)

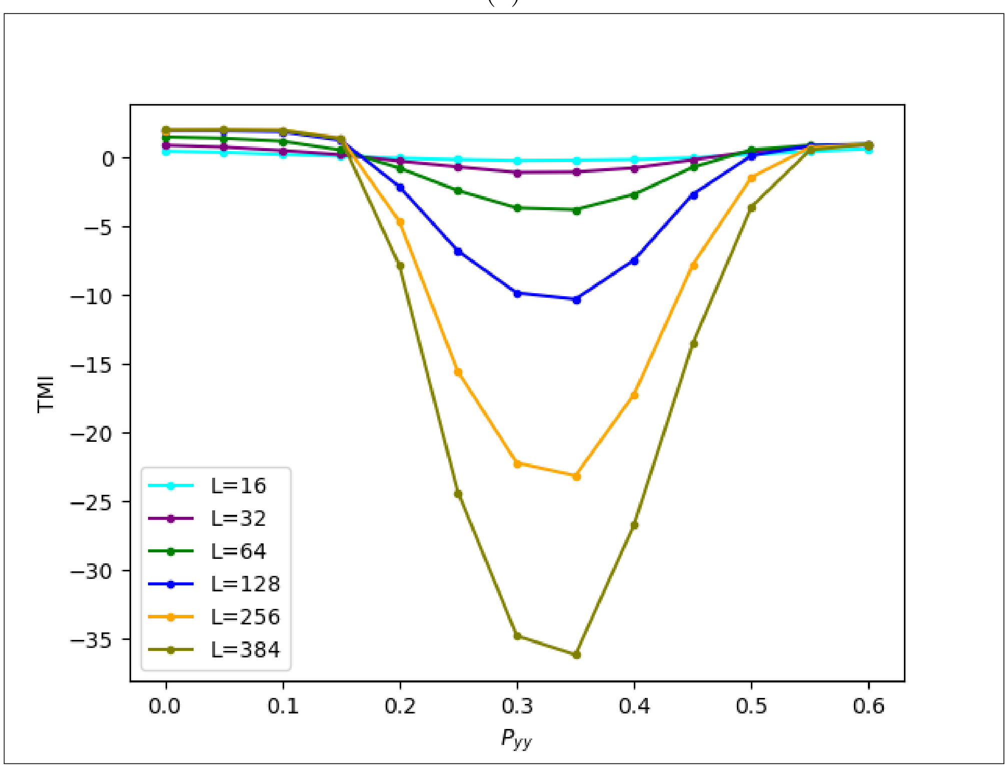

(b)

Figure 2: TMI vs P_{YY} with different values of α in the long-range measurements. The TMI is measured at $t = 40L$ up to the system size of $L = 384$ from $L = 16$ (light blue, purple, light green, thick blue, orange, and thick green, respectively) and averaged over 3000 outcomes with (a) $\alpha = 0.5$ and (b) $\alpha = 1.5$.

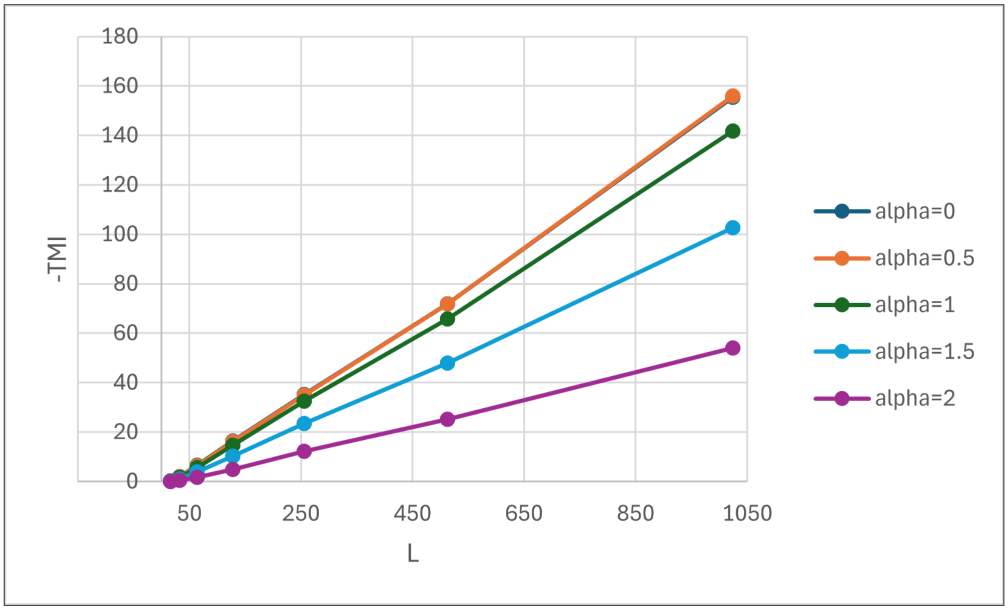

(a)

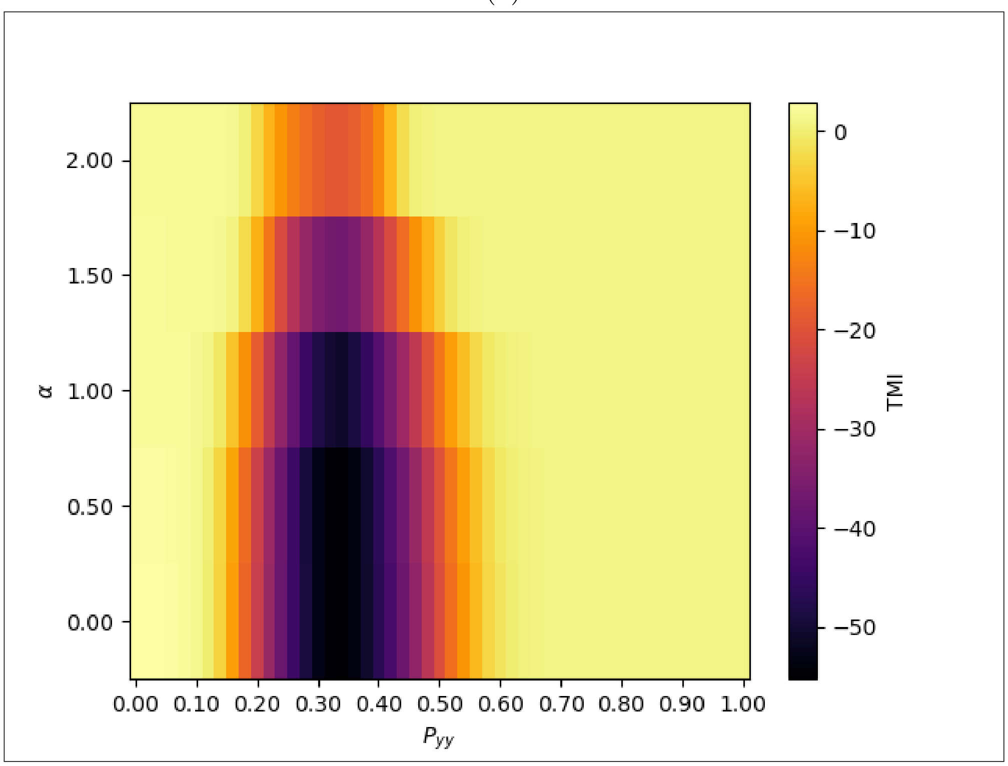

(b)

Figure 3: The density plot of TMI with respect to α and P_{YY} and linear dependence of $-TMI$ at equal probabilities of measurements.(c) Linear dependence of $-TMI$ over system size L at equal measurement probabilities $P_{XX} = P_{YY} = P_{ZZ} = \frac{1}{3}$ from $\alpha = 0, 0.5, 1.0, 1.5, 2.0$ in thick blue, orange, green, blue, and purple, respectively. (d) Density plot of TMI with $\alpha = 0, 0.5, 1.0, 1.5, 2.0$ at P_{YY} from 0 to 1.0. The data was taken at $t = 40L$ and with the system size of $L = 384$.

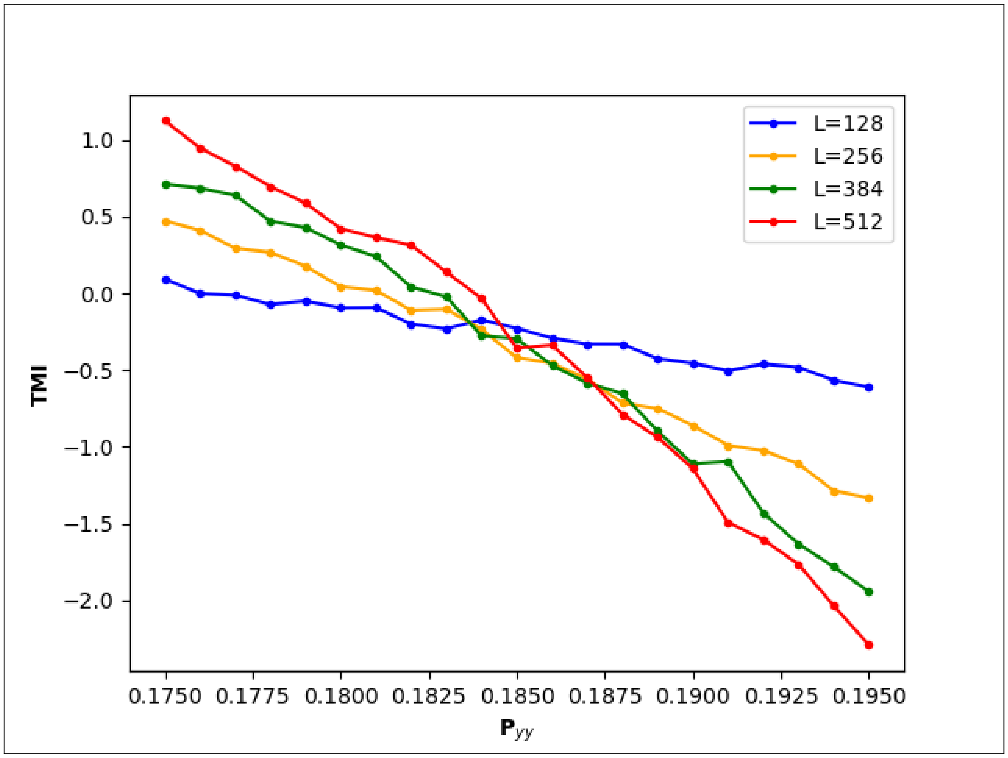

(a)

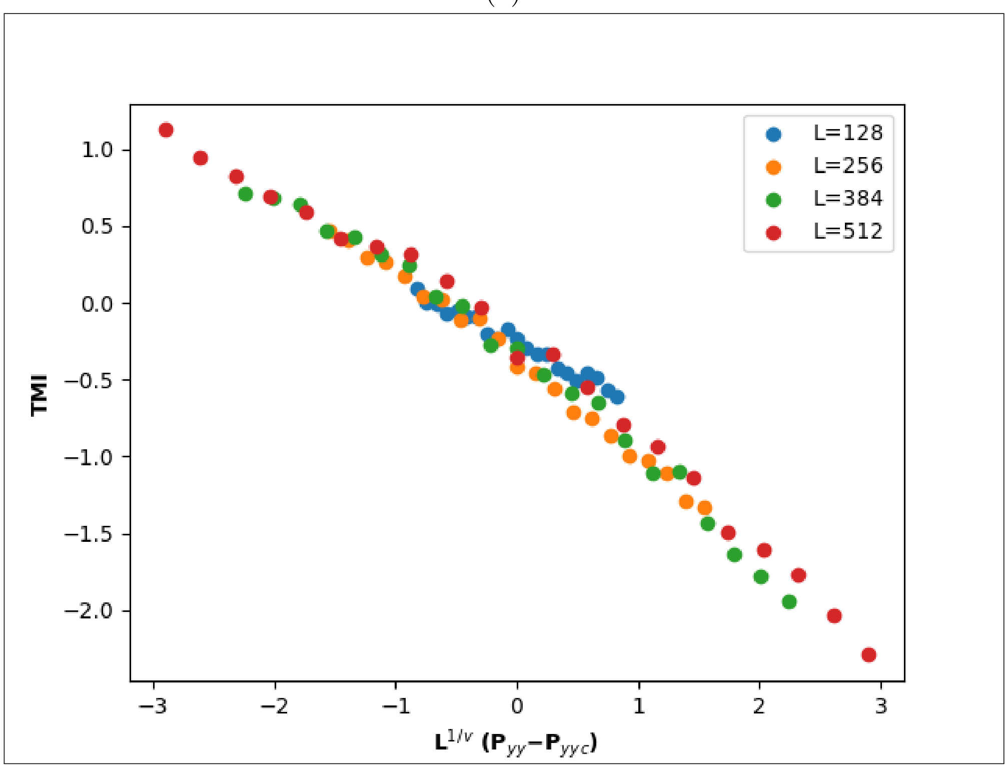

(b)

Figure 4: (a) The location of the transition point from the negative to the positive TMI region is found at $P_{YY} = 0.185$. The TMI is measured at $t = 40\ L$ up to the system size of $L = 512$ from $L = 128$ with $\alpha = 2.0$. (b) Finite-size scaling analysis is conducted with the data in Fig.4a. The TMI collapses when for a critical exponent $\nu = 1.1$ and $P_{YY} = 0.185$.

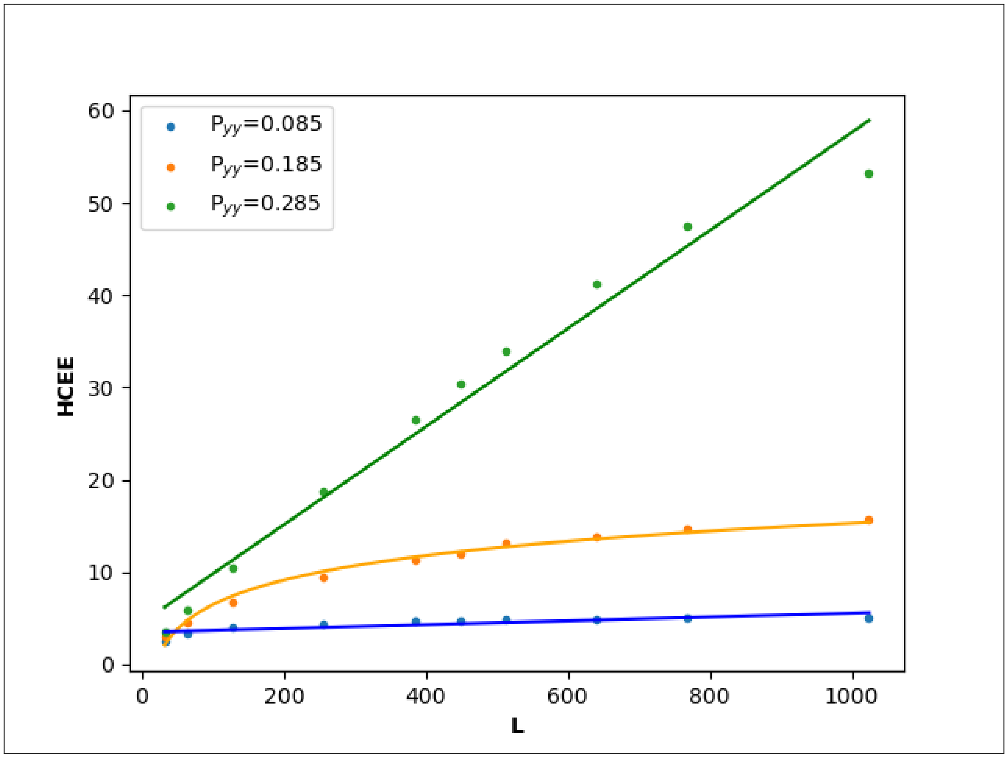

(a)

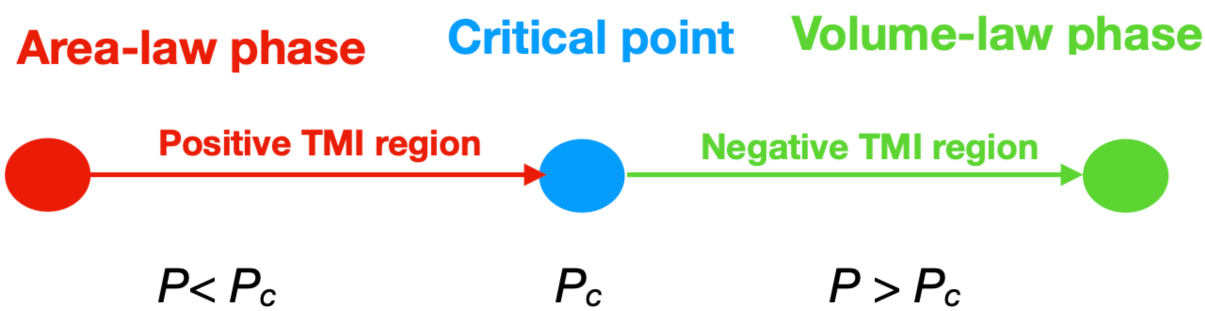

(b)

Figure 5: (a) HCEE vs L around the transition point at $t = 40L$. When P_{YY} increases HCEE shows more a linear relationship with the system size. The green,orange, and blue points (solid lines) are data (fitting curves). The volume-law (green) and intermediate-law(orange) follow linear and logarithmic scalings, respectively while area-law (blue) is independent of the system size. (b) A diagram of EPT in a relationship with TMI. The red, blue, and green colors represent area-law, dynamics at the critical point, and volume-law.

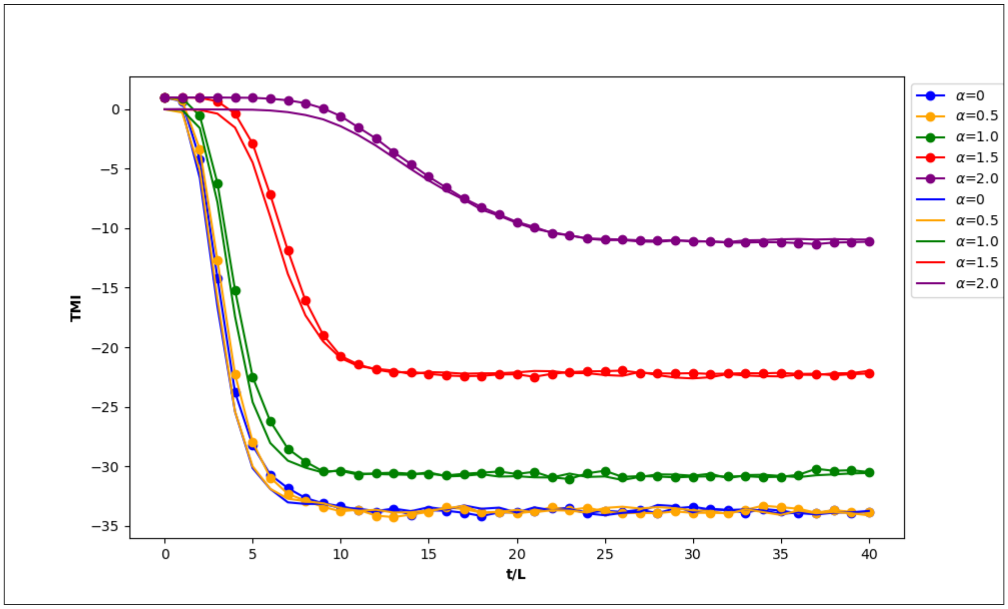

(a)

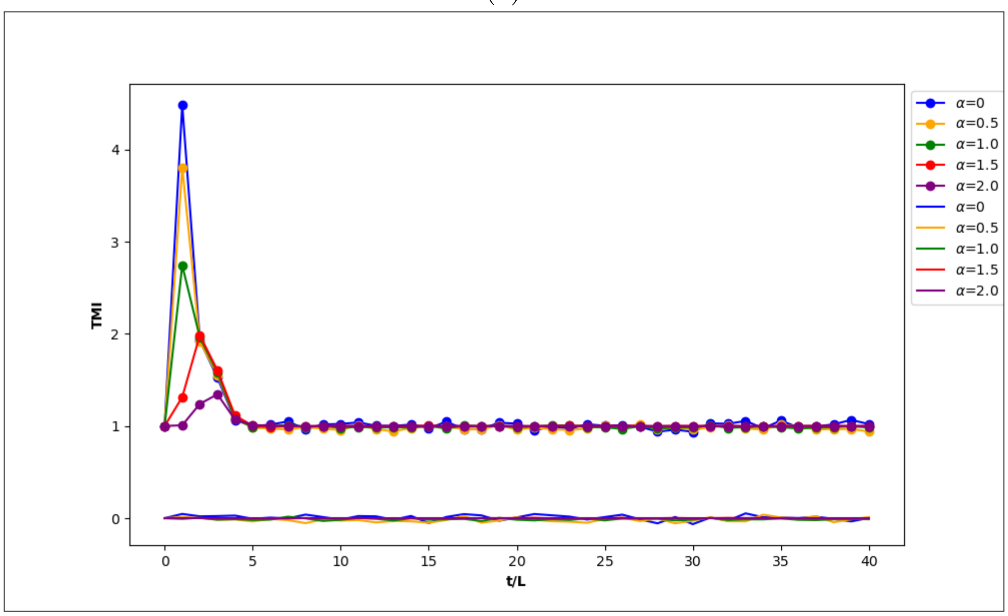

(b)

Figure 6: Initial state dependence of the MOC. The TMI is expanded over t with various α's at $L = 256$. The result is averaged over 3500 trajectories. The dashed line is the GHZ of the Z stabilizer states, and the solid line is and the product states. (a) There is no gap between these initial states at $P_{YY} = 0.3$. The solid line is product of X,Y, or Z initial states. (b) There is a gap of TMI by 1 at $P_{YY} = 0.7$. The solid line is the product of Y initial stabilizer states.

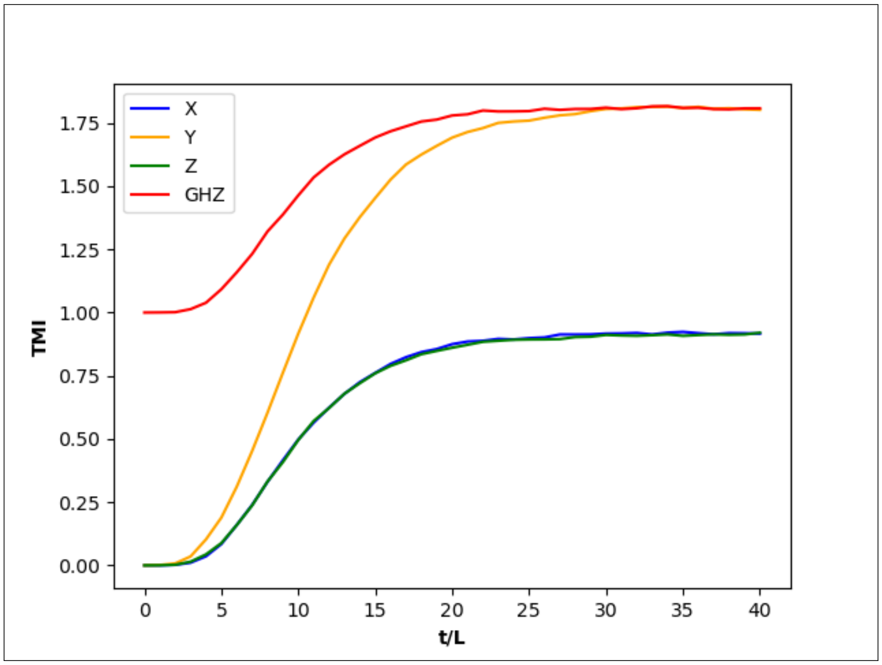

(a)

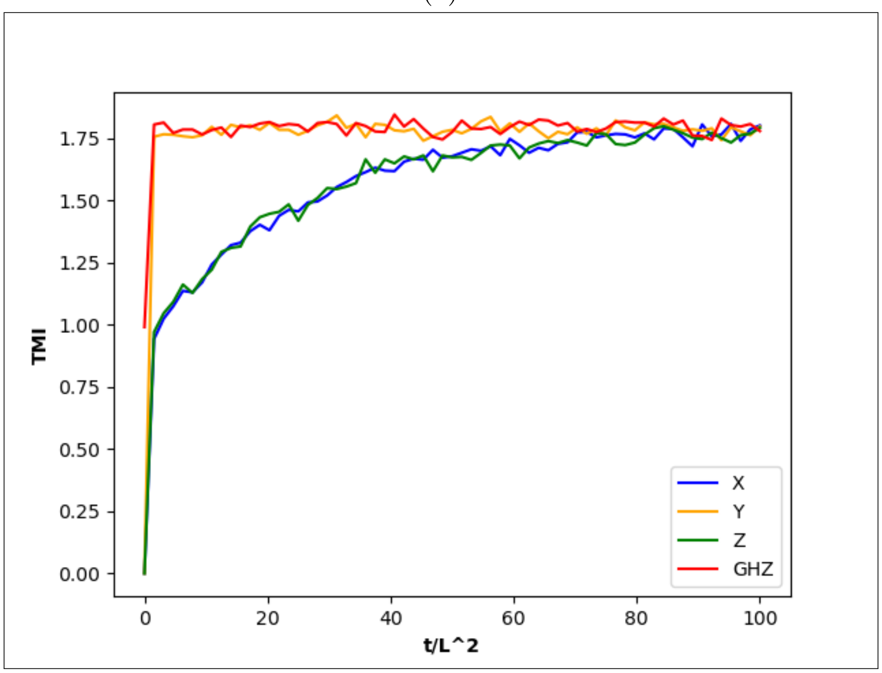

(b)

Figure 7: Long dynamics of TMI at $P_{YY} = 0.1$ with $\alpha = 2.0$. TMI is measured over $t = 40L$ (a) or $t = 100L^2$ (b) at $L = 256$ The blue, yellow, green, and red lines represent the results from the initial stabilizer states of X,Y,Z, and GHZ, respectively. (a) The initial entangled state contributes to 1 of TMI at $t = 40L$ while the initial product states do not. The gap remains during the short time expansion. The outcomes are averaged over 3500. (b) The gap vanishes after a long time of measurements. The time is expanded over $t = 100L^2$ at $L = 256$ and is averaged over 500 outcomes.

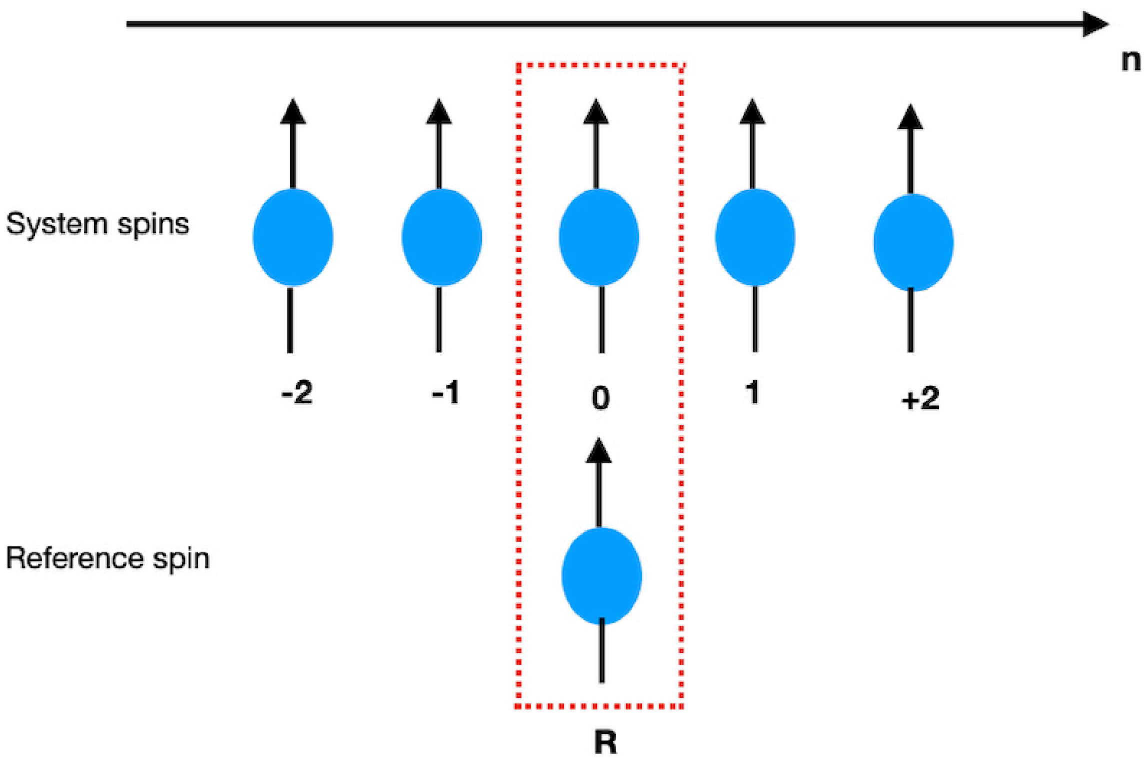

Figure 8: The setup of the scrambling measurement. We choose an isolated qubit denoted by **R** and make an EPR pair with 0-th qubit. We run the MOC without measuring the isolated qubit. All qubits except the reference qubit are prepared to be the Y initial stabilizer state.

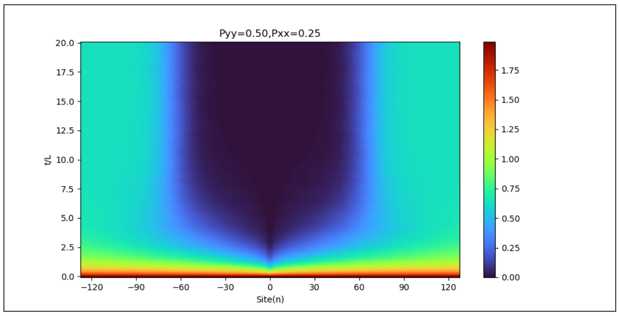

(a)

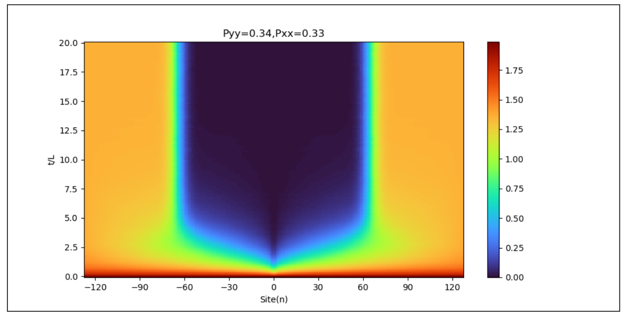

(b)

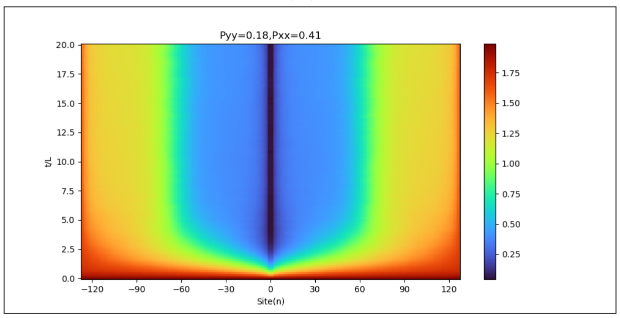

(c)

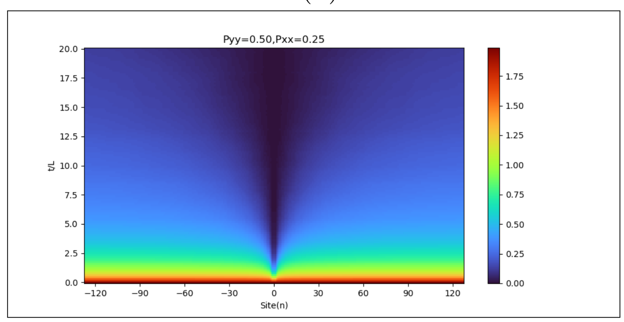

(d)

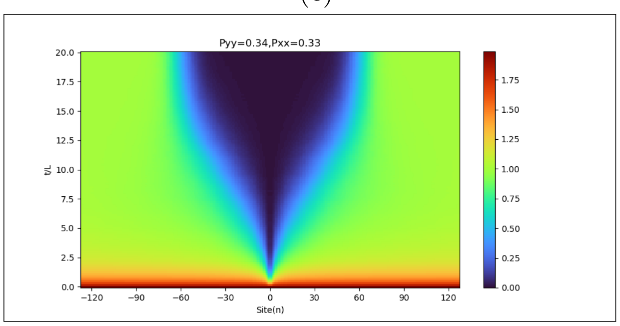

(e)

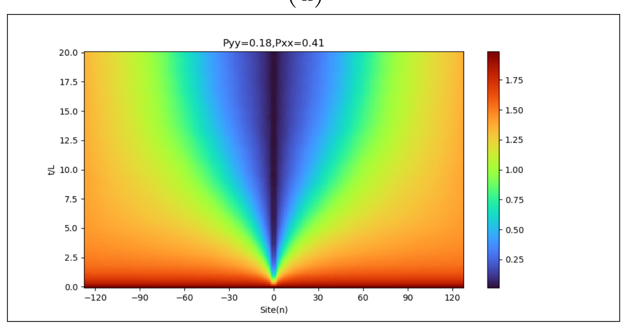

(f)

Figure 9: The density plot of the time evolution of the MI between the isolated spin and the entire system for each site in different conditions with $L = 256$. The results are averaged over 3000 realizations. When $t = 0$, all sites have the maximum MI of 2, where $0 \leq MI \leq 2$. The vertical axis is time steps relative to the chain length. The horizontal axis is the location of a spin relative to the center. (a,b,c) The density plot at $P_{YY} = 0.50, 0.34, 0.18$ and $\alpha = 1.0$, respectively.(d,e,f) The density plot at $P_{YY} = 0.50, 0.34, 0.18$ and $\alpha = 2.0$, respectively. a, b, e are in the volume law where we observe the propagation of quantum information, and c, d, f are in the area-law where we do not.

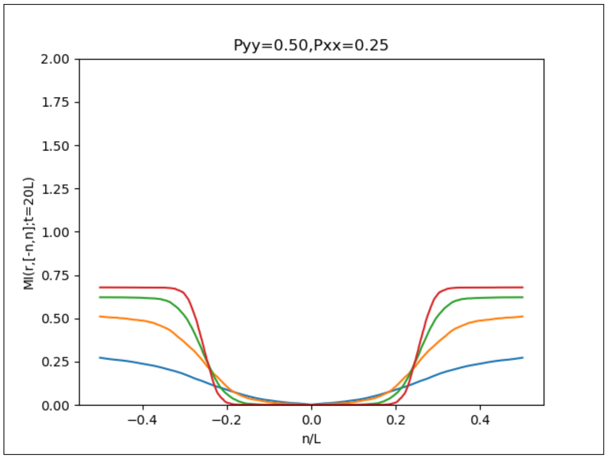

(a)

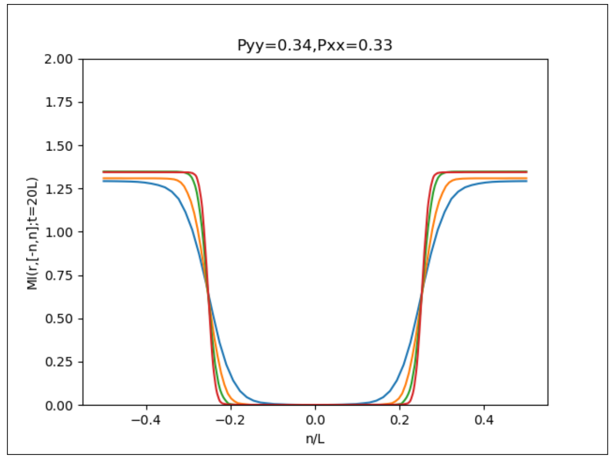

(b)

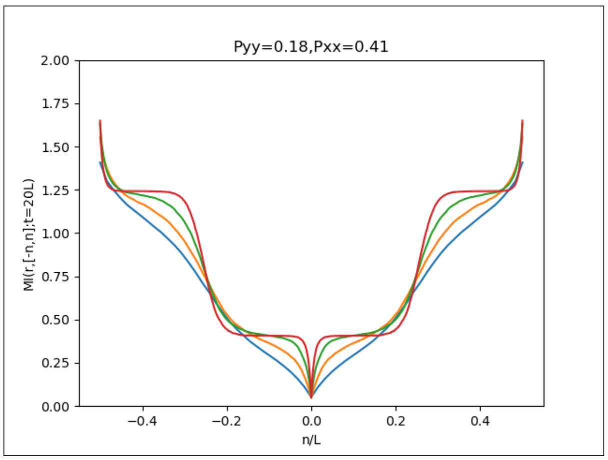

(c)

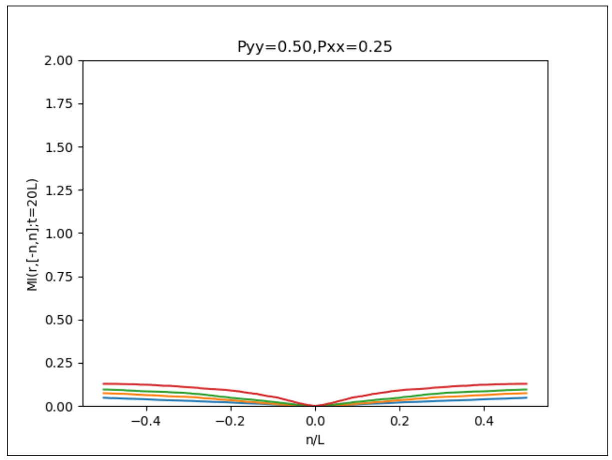

(d)

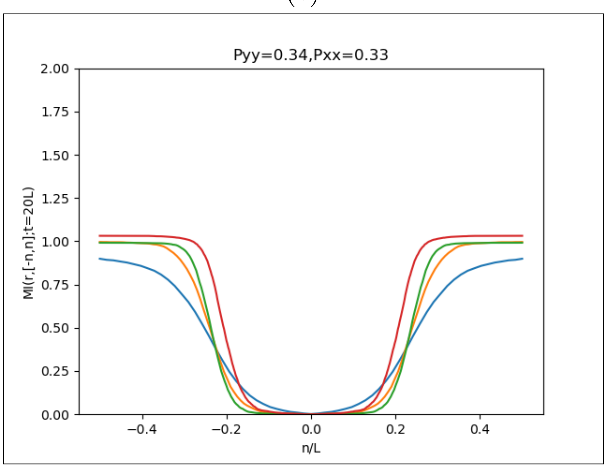

(e)

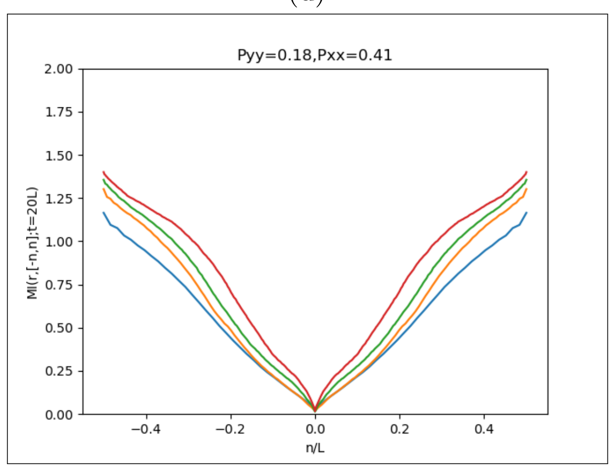

(f)

Figure 10: The saturated value of the MI between the isolated qubit and the entire system for each site for $L = 64, 128, 256$, and 512 conditions at $t = 20L$ (blue, orange, green, and red, respectively.) These results are averaged over 3500 realizations. The saturated value of the MI plot at $P_{YY} = 0.50, 0.34, 0.18$ and $\alpha = 1.0$, respectively (a,b,c) and $P_{YY} = 0.50, 0.34, 0.18$ and $\alpha = 2.0$,respectively(d,e,f).a,b, e are in the volume law where we observe scrambling, and c, d, f are in the area law where we do not.

V. DISCUSSION

In this work, we demonstrate many properties of the MOC through the quantities such as entanglement entropy, MI, and TMI. The long-range $XX/YY/ZZ$ MOC creates quantum correlation between qubits in the process of measurement and can be mapped into a unitary hybrid circuit which consists of $CNOT$ gates, CY gates, and each quantum gate (Appendix). This model transitions from the area-law to the volume-law at $P_{YY} = 0.185$ for $\alpha = 2.0$. This result suggests that $XX/YY/ZZ$ measurements can induce the EPT that is validated by finite-size scaling analysis. The entanglement entropy grows linearly or logarithmically if $p \geq p_c$ while it does not grow in area-law. At this transition point, we see that the signs of the TMI change from positive to negative. Here, positive (negative) TMI suggests weak (strong) entanglement over the entire system and such systems show the area-law (volume-law) entanglement. Suggested by Fig.3b, the magnitude of TMI gets larger as α decreases or $P_{yy} \to \frac{1}{3}$. The sign change of TMI is highly correlated to the EPT in the MOC.

Moreover, there is a connection to unitary black holes when the system is scrambled. The MOC acts as a 'unitary black hole' which suggests that quantum information is suddenly revealed if the system emits more than half of the entire entropy. We can interpret this phenomenon as that our model emits almost all quantum information after more than half of the spins are involved in measurement. This feature is captured as a step function of TMI in 4.3 Scrambling. However, we cannot see this effect in the area-law phase in which the information is localized rather than spread. This implies that if the system in MOC is in the volume-law phase, we can see scrambling suggested in IV. Results because the qubits in the phase are correlated together with larger spatial extension.

We also see the 'light cone' shapes in Fig. 9, which indicate the finite speed of quantum information scrambling. The magnitude of α in the volume-law region is related to the shapes of the 'light cone'. As α increases, the shape becomes sharper in the long-range measurement. It means that the speed of propagation of quantum information gets slower for larger α. In addition, if the system is in the volume-law phase and TMI is negative, we see the ‘light cone’ shape. In the short-range limit, $\alpha \to \infty$, the shape becomes more linear. However, the step function like behavior could not be seen, and the finite speed of the propagation is difficult to determine in our MOC due to the ambiguity. Our result indicates that long-range measurement significantly contributes to the shape of ’light cone‘ and the speed of quantum information.

VI. SUMMARY

Here is a summary of the key points discussed in this paper.

1. The long-range $XX/YY/ZZ$ MOC is implemented in the stabilizer formalism. The two-body measurements induce the EPTs and scrambling. Those results are calculated using quantities such as the entanglement entropy, $\boldsymbol{MI}$, and $\boldsymbol{TMI}$.

2. We see the EPT from the area-law to the volume-law with $P_{YY} = 0.185$ for $\alpha = 2.0$ and $\nu = 1.1$, which is validated by finite-size scaling analysis. At this transition point, the sign of the $\boldsymbol{TMI}$ changes from positive to negative. The entanglement growth in each phase is fitted with numerical technique.

3. This model has the initial state dependence of $\boldsymbol{TMI}$ when we choose the product of the Y initial stabilizer states with $P_{YY} \geq 0.5$. This initial state takes a longer time to contribute to the $\boldsymbol{TMI}$ by 1 due to the low probabilities of other measurements. However, the gap of $\boldsymbol{TMI}$ vanishes after a long time of measurements.

4. We notice the propagation of quantum information, which is measured by the $\boldsymbol{MI}$ between the isolated qubit and the entire system. We can see scrambling effects in the volume-law phase due to the strong correlation between the qubits. We notice that the propagation of the quantum information is shaped as ‘light cones’, and it becomes sharper as α increases in the long-range measurements.

5. There is a connection to a unitary black hole when the MOC is scrambled. In the volume-law phase the MOC reveals almost all quantum information once more than half the spins are involved in measurements. This behavior is seen as a step function of the saturated value of the $\boldsymbol{MI}$ in Fig. 10.

APPENDIX

A.1 Mapping to hybrid circuit

We can map the MOC into a hybrid unitary circuit which is composed by a $CNOT$ gate, a controlled Y gate, and measurements. The transformation of each two-body measurement is as follows:

$$X_iX_j = U_{ij}^{\dagger}X_iU_{ij}. \tag{18}$$

$$Y_iY_j = (CY)_{ij}^{\dagger}Y_i(CY)_{ij}. \tag{19}$$

$$Z_iZ_j = U_{ij}^{\dagger}Z_jU_{ij}. \tag{20}$$

where U_{ij} is a $CNOT$ gate with a control qubit of i and a target qubit of j and CY_{ij} is a controlled Y gate.

A.2 Half Chain Entanglement Entropy

Half chain entanglement entropy (HCEE) denoted by $S_{\frac{L}{2}}$, is bipartite entanglement in which the subsystems are equally divided at the center of the one-dimensional spin chain. We use HCEE to determine the strength of the entanglement entropy. In Clifford evolution, the Von Neumann entropy $S(x,t)$ evolved from a product state to a near-maximally-entangled state. The entropy saturates to a triangle-like shape that represents close to the maximum entanglement(29). In Fig.11a, we see the relationship between HCEE and L with the same probabilities of each measurement at $t = 40L$. Not only the probabilities of the measurement but also the strength of the parameter of α can affect the entanglement growth in the MOC. Fig. 11b shows the bipartite entanglement entropy of $S(x,t)$ for successive times in a system of $L = 459$ where x is a size of the subsystem. At very late times, $S(x,t)$ saturates to a pyramid-like shape at $x \approx 225$ which represents maximum entanglement entropy. To maximize the bipartite entanglement entropy, we chose subsystems which are equally divided at the center of the one-dimensional spin chain (HCEE).

A.3 Finite-size scaling analysis

Consider a system with a parameter ρ, in which there is a phase transition at a parameter ρ_c. The correlation length ξ diverges, which characterizes the critical point in infinite system. As the correlation length diverges as $\xi \approx |\rho-\rho_c|^{-\nu}$ for $\rho \to \rho_c$ where ˇ is critical exponent and describes the divergence of typical length scale(31), we have

$$A_L(\rho) \approx |\rho-\rho_c|^{-\zeta}, (L \gg \zeta \text{and} \rho \to \rho_c), \tag{21}$$

where ζ is some critical exponent. For $L \ll \xi$ and $\rho \to \rho_c$ we expect

$$A_L \approx L^{\frac{\zeta}{\nu}}. \tag{22}$$

These compose the finite scaling ansatz

$$A_L(\rho) = \xi^{\zeta/\nu} f(L/\xi), \quad (L \to \infty, \rho \to \rho_c),$$

with

$$f(x) = \begin{cases} \text{const.} & \text{for } |x| \gg 1, \\ \sim x^{\zeta/\nu} & \text{for } x \to 0. \end{cases}$$

The scaling function of $f(x)$ is dimensionless function. The conventional scaling function is $F(x) = x^{-\zeta} f(x^{\nu})$ (32), such that

$$A_L(\rho) = L^{\zeta/\nu} F(L^{1/\nu}(\rho-\rho_c)), \quad (L \to \infty, \rho \to \rho_c),$$

with

$$F(x) = \begin{cases} \text{const.} & \text{for } x \to 0\,(L \ll \xi), \\ \sim L^{-\zeta/\nu}(\rho-\rho_c)^{-\zeta} & \text{for } |x| \gg 1\,(L \gg \xi). \end{cases}$$

In this work, we apply the data data collapse method, using the conventional scaling function Eqn.16.

$$F(L^{1/\nu}(\rho-\rho_c)) = L^{-\zeta/\nu}A_L(\rho).$$

where $\zeta = -1$. The data collapses with the right choice of ν, ζ for the parameter of ρ_c. We utilize the Python package of `Pyfssa` to get the result.

A.4 Supplemental data for initial state dependence

The initial state dependence of the GHZ of Z state compared to the product of the Y initial stabilizer state is shown in Fig.13. The difference in the TMI by 1 is seen when $P_{YY} \geq 0.5$ due to the low probabilities of other projective measurements. This means that forming clusters of X and Z stabilizer states takes longer than ones with $P_{YY} < 0.5$. We see peaks with low P_{YY} ($P_{YY} = 0, 0.1$) and high P_{YY} ($P_{YY} = 0.6, 0.7, 0.8, 0.9, 1.0$). For low P_{YY}, the clusters of the stabilizer states X and Z form rapidly, and the size of the clusters that include the stabilizer state Y is proportional to the probability distributions. For high P_{YY}, the cluster of the Y initial stabilizer states is made rapidly instead of the X and Z stabilizer states. The final states are similarly proportional to the probability distribution.

A.5 Supplemental data for scrambling

We have plotted the time evolution of the MI with $\alpha = 0, 0.5, 1.5, 2.5, 3.0, 3.5$ at $P_{XX} = P_{YY} = P_{ZZ} = \frac{1}{3}$ and the saturated value with $\alpha = 0.5, 1.5$ under the same conditions described in IV. Results. Fig.14 shows the time evolution of the MI in the measurements of the qubits without the reference qubit. We see the 'light cone' in the volume region according to Appendix in Fig.14b and Fig.14c. The quantum information spreads logarithmically for $\alpha = 0, 0.5$ while it propagates more linearly for $\alpha = 1.5$. This means that tuning the distance of the measurements increase or decrease the speed of propagation of quantum information.

In contrast, the shapes of other figures in the long-range measurements ($\alpha > 2$) do not indicate scrambling or the 'light cone'. This leads to the localization of information instead of scrambling in the short range measurements. In addition, Fig.15 shows the saturated values of the MI at $t = 20L$. Fig.15a, Fig.15b, and Fig.15e are shaped as step functions, which indicate that the quantum information propagates all over the regions. Fig.15f shows the intermediate feature of scrambling since the system experiences the dynamical transition from the area-law to the volume phases with the probability distribution. Fig.15c and Fig.15f show that the system is in the MBL phase and is not thermalized. The quantum information is localized.

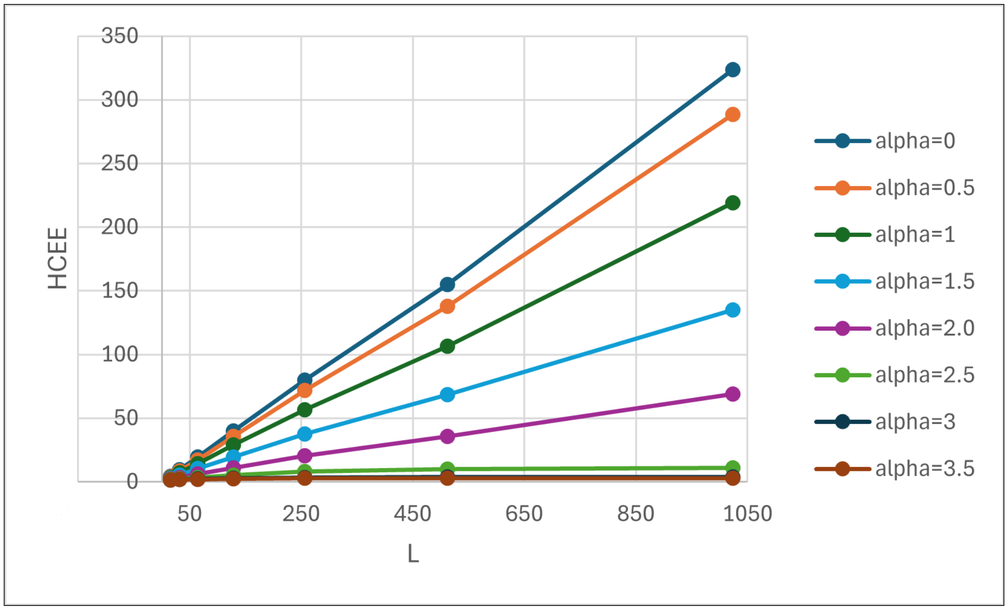

(a)

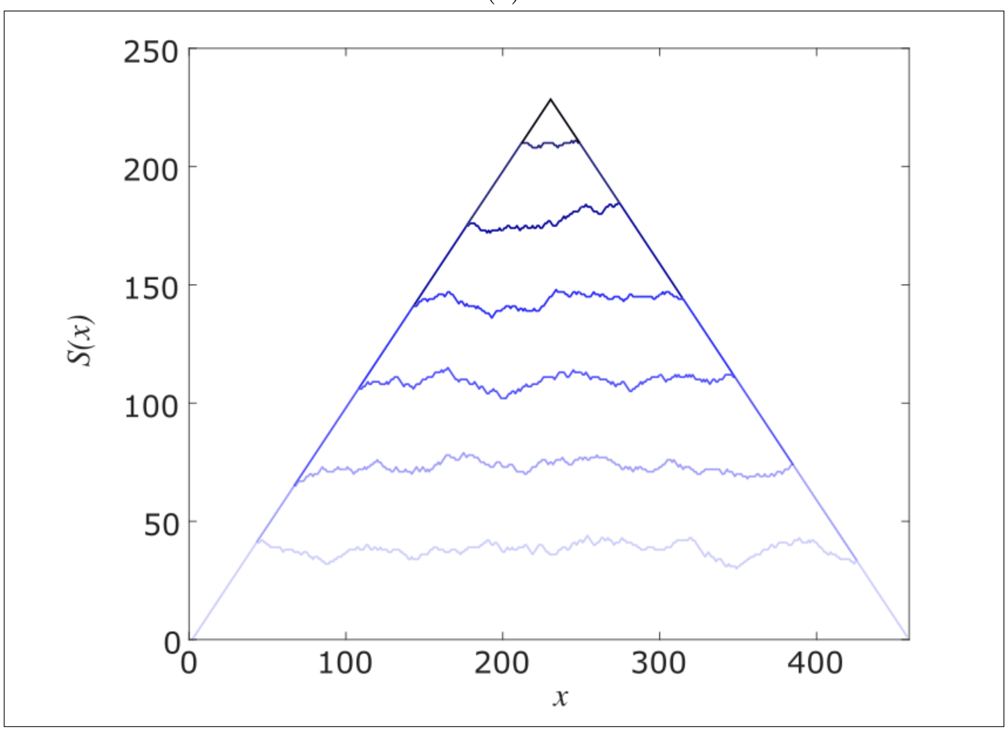

(b)

Figure 11: (a)HCEE vs system size. (b) Bipartite von Neuman entropy $S(x,t)$ taken from (29). (a) Blue, orange, thick green, light blue, purple, light green, thick blue, and brown represent the parameter from $\alpha = 0$ to $\alpha = 3.5$ with probabilities $P_{XX} = P_{YY} = P_{ZZ} = \frac{1}{3}$ at $t = 40L$,respectively. $S_{\frac{L}{2}}$ for long-range measurements shows the volume law entanglement while $S_{\frac{L}{2}}$ for short-range measurements shows the area law entanglement. (b) The von Neuman entropy, $S(x,t)$ for a system length of $L = 459$ for several successive times ($t = 340, 690, 1024, 1365, 1707, 2048, \text{and} 4096$),

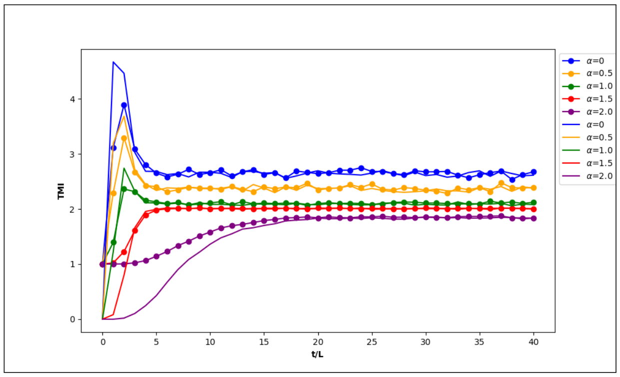
TMI
t/L
α=0
α=0.5
α=1.0
α=1.5
α=2.0
α=0
α=0.5
α=1.0
α=1.5
α=2.0

(a)

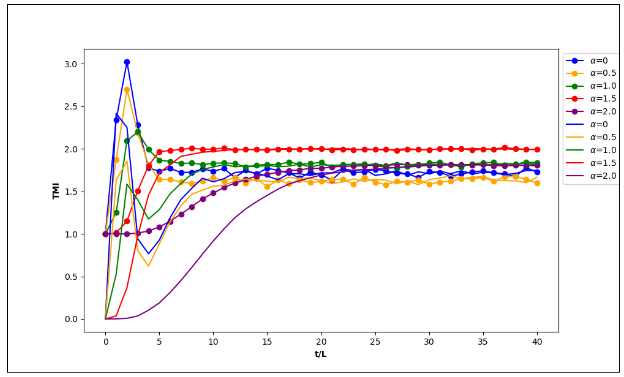
TMI
t/L
α=0
α=0.5
α=1.0
α=1.5
α=2.0
α=0
α=0.5
α=1.0
α=1.5
α=2.0

(b)

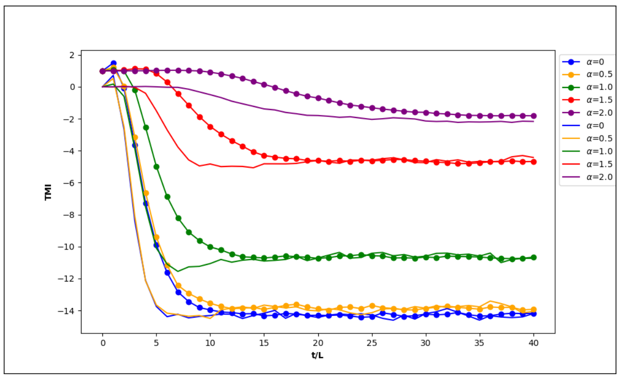
TMI
t/L
α=0
α=0.5
α=1.0
α=1.5
α=2.0
α=0
α=0.5
α=1.0
α=1.5
α=2.0

(c)

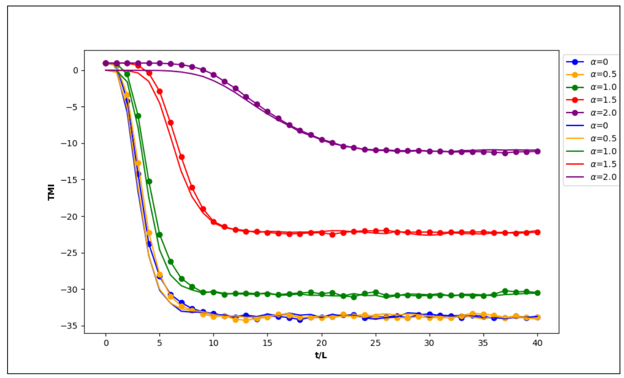
TMI
t/L
α=0
α=0.5
α=1.0
α=1.5
α=2.0
α=0
α=0.5
α=1.0
α=1.5
α=2.0

(d)

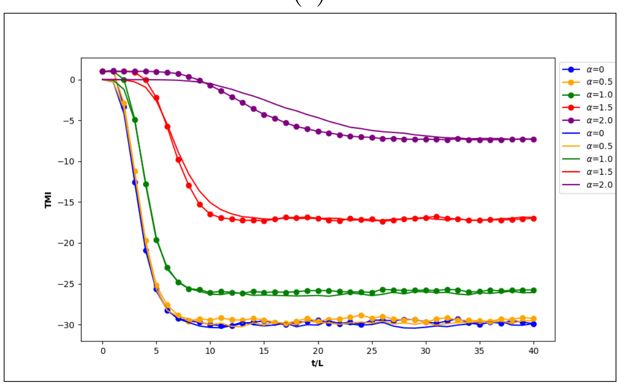
TMI
t/L
α=0
α=0.5
α=1.0
α=1.5
α=2.0
α=0
α=0.5
α=1.0
α=1.5
α=2.0

(e)

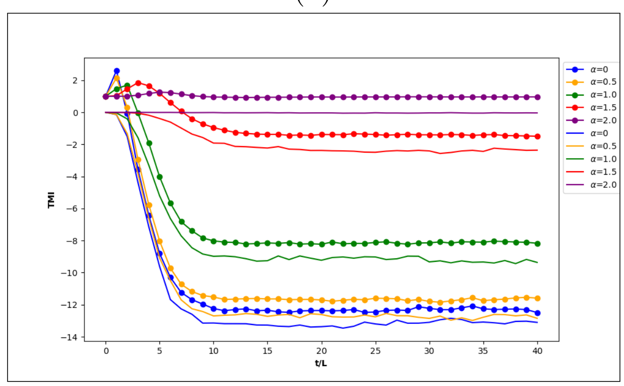
TMI
t/L
α=0
α=0.5
α=1.0
α=1.5
α=2.0
α=0
α=0.5
α=1.0
α=1.5
α=2.0

(f)

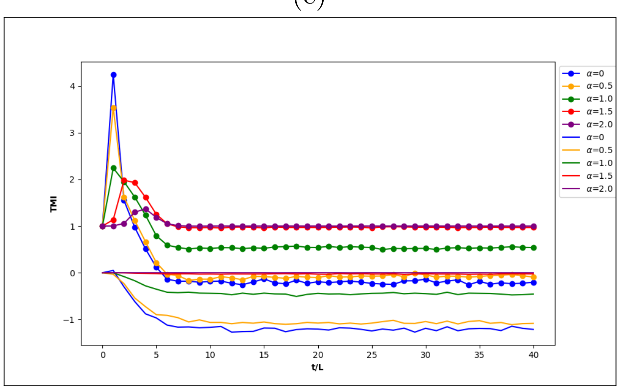
TMI
t/L
α=0
α=0.5
α=1.0
α=1.5
α=2.0
α=0
α=0.5
α=1.0
α=1.5
α=2.0

(g)

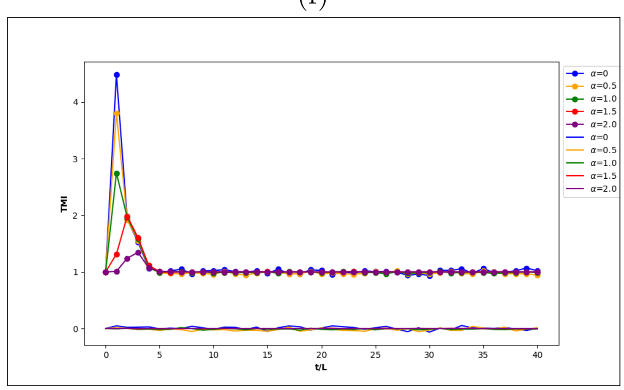
TMI
t/L
α=0
α=0.5
α=1.0
α=1.5
α=2.0
α=0
α=0.5
α=1.0
α=1.5
α=2.0

(h)

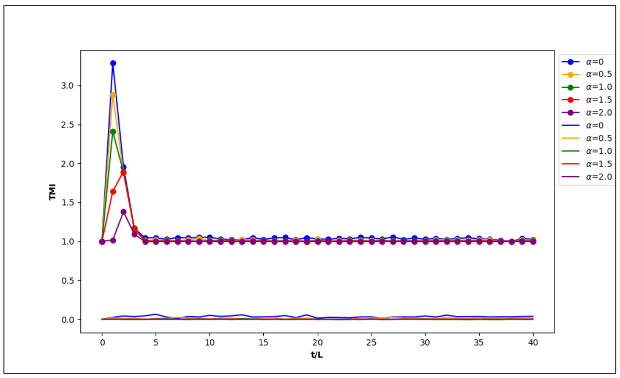

(i)

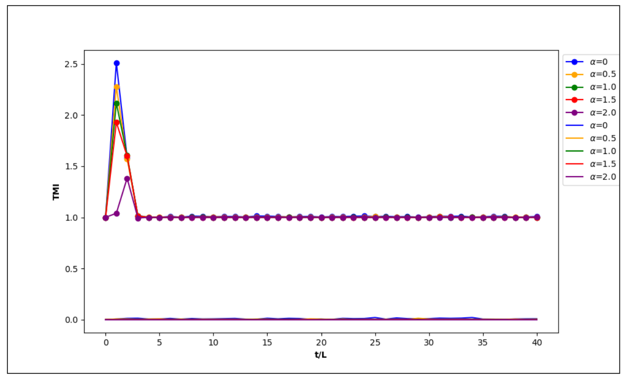

(j)

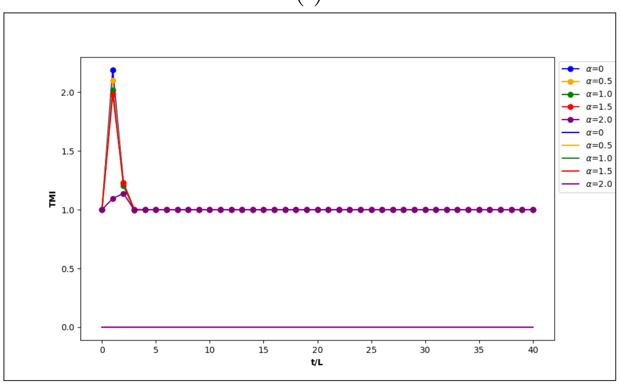

(k)

Figure 13: The initial state dependence of the GHZ of Z state in comparison with the Y initial stabilizer state. We plot the dynamics of TMI up to $t = 40L$ in the short-range measurements. The blue, yellow, green, red ,and purple correspond to the degrees of α from $\alpha = 0$ to $\alpha = 2.0$, respectively. The solid line is the Y initial stabilizer state and the dashed line is the GHZ of Z stabilizer state.(a-k)The probabilities are $P_{YY} = 0, 0.1, 0.2, 0.3, 0.4, 0.5, 0.6, 0.7, 0.8, 0.9, 1.0$, respectively. The TMI gap by 1 occurs when $P_{YY} \geq 0.5$.

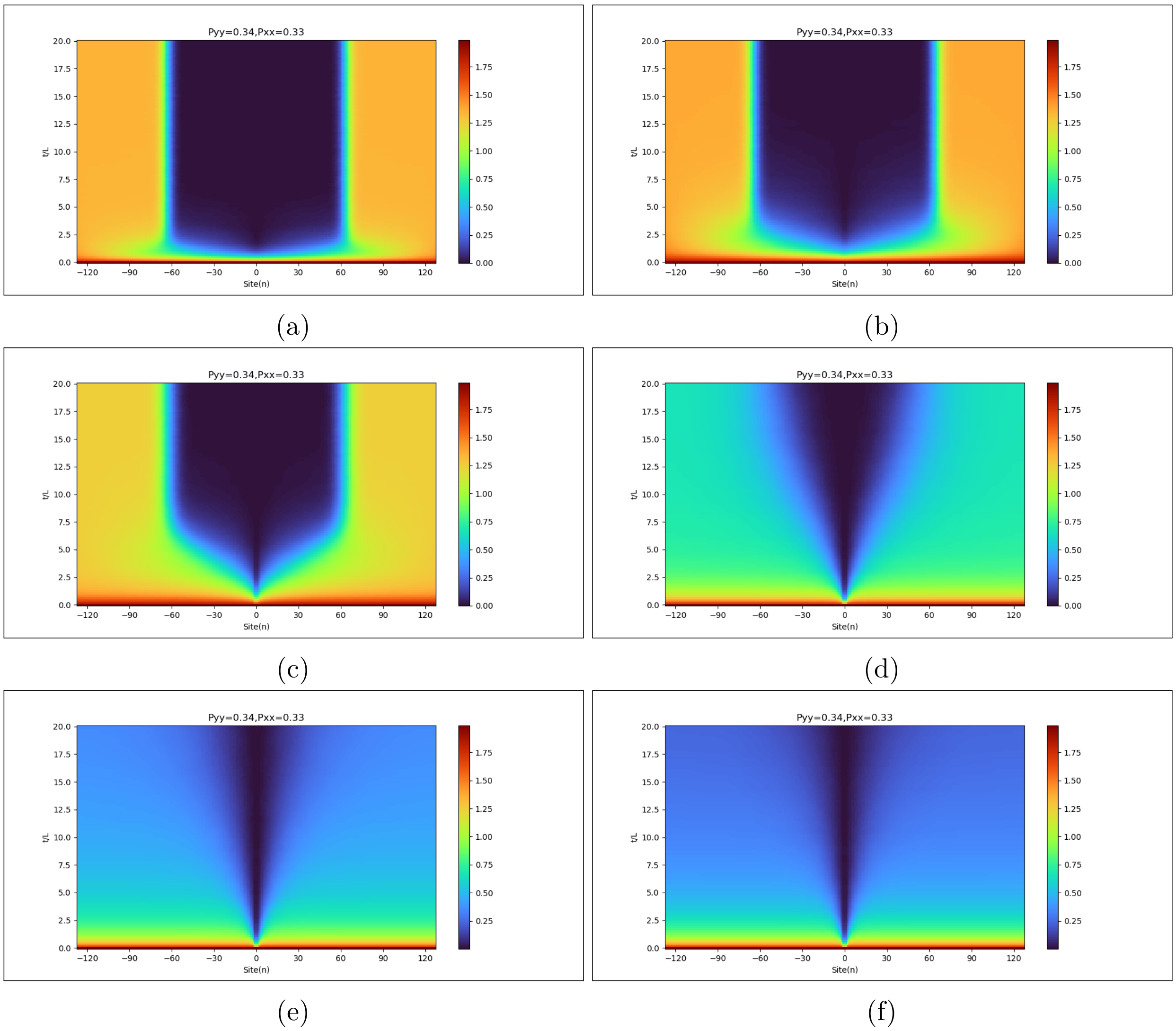

Figure 14: The density plot of the time evolution of the MI between the isolated spin and the entire system for each site in different conditions with $L = 256$. The results are averaged over 3000 realizations. When $t = 0$, all sites have the maximum MI of 2, where $0 \leq MI \leq 2$. The vertical axis is time steps relative to the chain length. The horizontal axis is the location of a spin relative to the center. (a,b,c,d,e) The density plot at $P_{XX} = P_{YY} = P_{ZZ} = \frac{1}{3}$ with $\alpha = 0, 0.5, 1.5, 2.5, 3.0, 3.5$, respectively. The shape of the 'light cone' becomes sharper as α increases in the long-range measurements ($\alpha \leq 2.0$). However, the quantum information is localized when $\alpha > 2.0$.

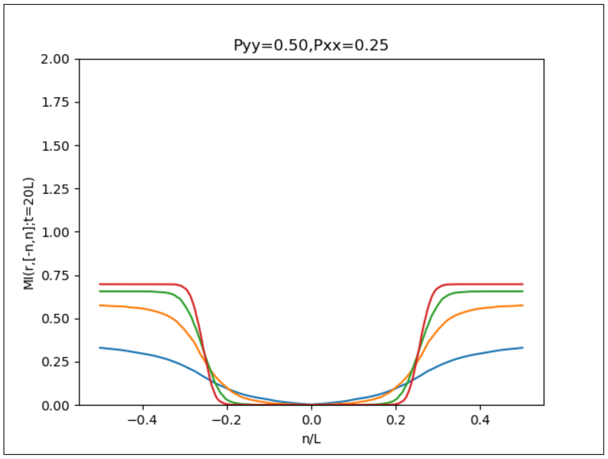

(a)

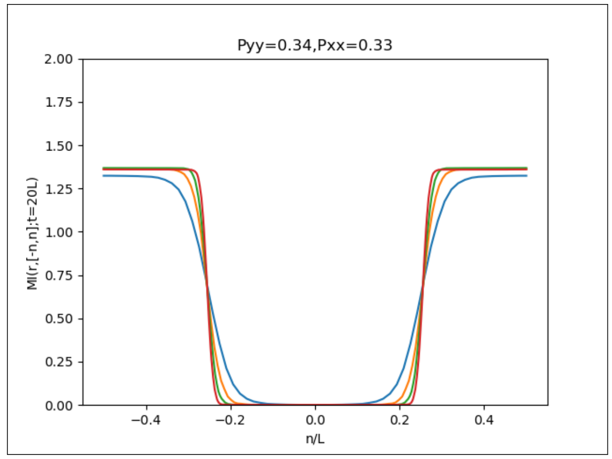

(b)

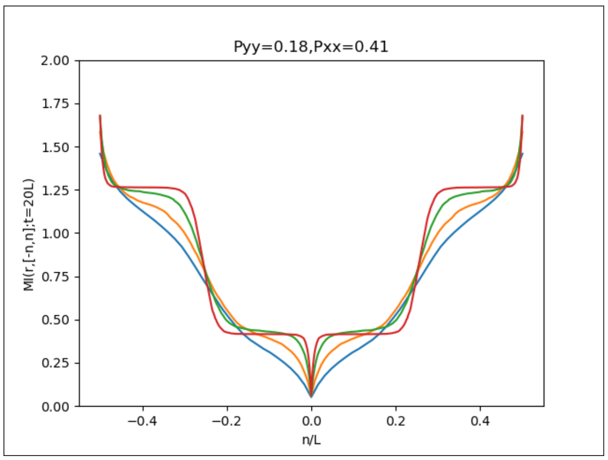

(c)

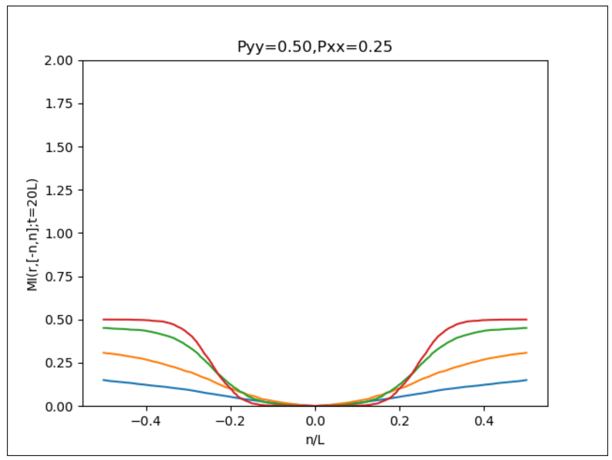

(d)

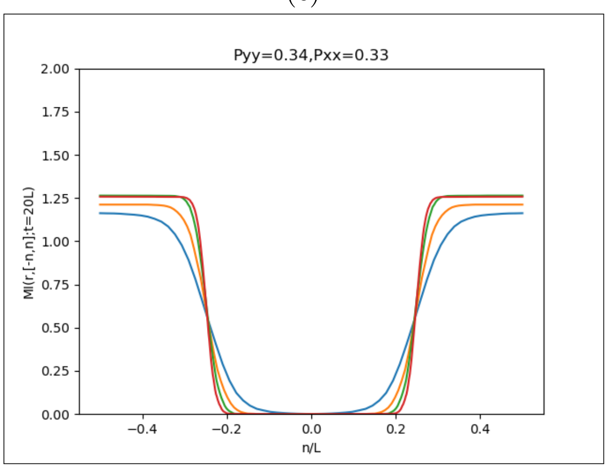

(e)

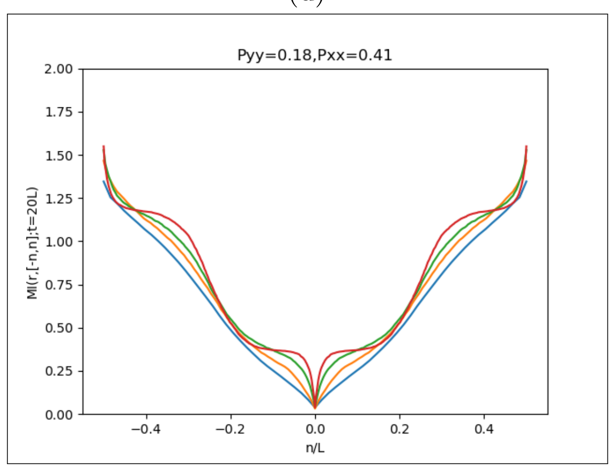

(f)

Figure 15: The saturated value of the MI between the isolated qubit and the entire system for each site for $L = 64, 128, 256$, and 512 conditions at $t = 20L$ (blue, orange, green, and red, respectively.) These results are averaged over 3500 realizations. The saturated value of the MI plot with $P_{YY} = 0.50, 0.34, 0.18$ and $\alpha = 0.5$, respectively (a,b,c) and $P_{YY} = 0.50, 0.34, 0.18$ and $\alpha = 1.5$, respectively(d,e,f).a, b, d, e are in the volume law where we observe scrambling, and c, f are in the area law where we do not.

REFERENCES

[1] B. Skinner, J. Ruhman, and A. Nahum. Measurement-induced phase transitions in the dynamics of entanglement. Phys. Rev. X, 9:031009, 2019.

[2] Romain Vasseur, Andrew C. Potter, Yi-Zhuang You, and Andreas W. W. Ludwig. Entanglement transitions from holographic random tensor networks. Physical Review B, 100(13), October 2019.

[3] Yoshihito Kuno, Takahiro Orito, and Ikuo Ichinose. Phase transition and evidence of fast-scrambling phase in measurement-only quantum circuits. Physical Review B, 108(9):094104, 2023.

[4] Patrick Hayden and John Preskill. Black holes as mirrors: quantum information in random subsystems. Journal of High Energy Physics, 2007(09):120–120, September 2007.

[5] Matteo Ippoliti, Michael J Gullans, Sarang Gopalakrishnan, David A Huse, and Vedika Khemani. Entanglement phase transitions in measurement-only dynamics. Physical Review X, 11(1):011030, 2021.

[6] Yaodong Li, Xiao Chen, Andrew W. Ludwig, Hong-Chen Jiang, Zhenyu Guo, and Xiao-Liang Qi. Measurement-driven entanglement transition in hybrid quantum circuits. arXiv preprint arXiv:1806.02807, 2018. Accepted in Physical Review B.

[7] Chao-Ming Jian, Yi-Zhuang You, Romain Vasseur, and Andreas W. W. Ludwig. Measurement-induced criticality in random quantum circuits. Phys. Rev. B, 101:104302, Mar 2020.

[8] Yaodong Li, Xiao Chen, Andreas WW Ludwig, and Matthew PA Fisher. Conformal invariance and quantum nonlocality in critical hybrid circuits. Physical Review B, 104(10):104305, 2021.

[9] Joshua D. Qualls. Lectures on conformal field theory, 2016.

[10] Vinod KS Shante and Scott Kirkpatrick. An introduction to percolation theory. Advances in Physics, 20(85):325–357, 1971.

[11] Johannes Hauschild and Frank Pollmann. Efficient numerical simulations with tensor networks: Tensor network python (tenpy). SciPost Physics Lecture Notes, October 2018.

[12] J. M. Deutsch. Quantum statistical mechanics in a closed system. Phys. Rev. A, 43:2046–2049, Feb 1991.

[13] Mark Srednicki. Chaos and quantum thermalization. Phys. Rev. E, 50:888–901, Aug 1994.

[14] Anna Goremykina, Romain Vasseur, and Maksym Serbyn. Analytically solvable renormalization group for the many-body localization transition. Phys. Rev. Lett., 122:040601, Jan 2019.

[15] Bela Bauer and Chetan Nayak. Area laws in a many-body localized state and its implications for topological order. Journal of Statistical Mechanics: Theory and Experiment, 2013(09):P09005, September 2013.

[16] Steven H. Strogatz. Nonlinear Dynamics and Chaos: With Applications to Physics, Biology, Chemistry, and Engineering. CRC Press, Boca Raton, FL, 2nd edition, 2018.

[17] Yasuhiro Sekino and Leonard Susskind. Fast scramblers. Journal of High Energy Physics, 2008(10):065, 2008.

[18] K. A. Landsman, C. Figgatt, T. Schuster, N. M. Linke, B. Yoshida, N. Y. Yao, and C. Monroe. Verified quantum information scrambling. Nature, 567(7746):61–65, March 2019.

[19] Daniel A. Roberts, Douglas Stanford, and Leonard Susskind. Localized shocks. Journal of High Energy Physics, 2015(3), March 2015.

[20] Elliott H. Lieb and Derek W. Robinson. The finite group velocity of quantum spin systems. Communications in Mathematical Physics, 28:251–257, 1972.

[21] Stanley J Brodsky, Hans-Christian Pauli, and Stephen S Pinsky. Quantum chromodynamics and other field theories on the light cone. Physics Reports, 301(4-6):299–486, 1998.

[22] Minh C. Tran, Andrew Y. Guo, Christopher L. Baldwin, Adam Ehrenberg, Alexey V. Gorshkov, and Andrew Lucas. Lieb-robinson light cone for power-law interactions. Physical Review Letters, 127(16), October 2021.

[23] Ron Belyansky, Przemyslaw Bienias, Yaroslav A. Kharkov, Alexey V. Gorshkov, and Brian Swingle. Minimal model for fast scrambling. Phys. Rev. Lett., 125:130601, Sep 2020.

[24] Scott Aaronson and Daniel Gottesman. Improved simulation of stabilizer circuits. Physical Review A, 70(5), November 2004.

[25] Charles H. Bennett, David P. DiVincenzo, John A. Smolin, and William K. Wootters. Mixed-state entanglement and quantum error correction. Physical Review A, 54(5):3824–3851, November 1996.

[26] Alastair Kay Chiara Macchiavello Artur Ekert, Timothy Hosgood. Introduction to quantum information science, n.d. Accessed: 2024-12-25.

[27] Daniel Gottesman. The heisenberg representation of quantum computers. arXiv preprint quant-ph/9807006, 1998.

[28] Koenraad M R Audenaert and Martin B Plenio. Entanglement on mixed stabilizer

states: normal forms and reduction procedures. New Journal of Physics, 7:170–170, August 2005.

[29] Adam Nahum, Jonathan Ruhman, Sagar Vijay, and Jeongwan Haah. Quantum entanglement growth under random unitary dynamics. Physical Review X, 7(3):031016, 2017.

[30] Hrant Gharibyan and Robert F. Penna. Are entangled particles connected by wormholes? Physical Review D, 89(6), March 2014.

[31] O. Melchert. autoscale.py - a program for automatic finite-size scaling analyses: A user's guide, 2009.

[32] M. E. J. Newman and G. T. Barkema. Monte Carlo Methods in Statistical Physics. Oxford University Press, 1999.